Research paper

Multiscale modeling of coupled thermo-mechanical behavior of granular media in large deformation and flow

Shiwei Zhao [a,b,*], Jidong Zhao [a,c,*], Weijian Liang [a], Fujun Niu [b]

[a] Department of Civil and Environmental Engineering, The Hong Kong University of Science and Technology, Clearwater Bay, Hong Kong SAR, China
[b] South China Institute of Geotechnical Engineering, South China University of Technology, Guangzhou, China
[c] HKUST Shenzhen-Hong Kong Collaborative Innovation Research Institute, Futian, Shenzhen, China

ARTICLE INFO

ABSTRACT

Heat generation and transfer in a granular material can be intricately coupled with their mechanical responses, playing a key role in causing excessive large deformation, flow and failure of the material. The coupling may manifest in various forms, including thermal induced stress, mechanically induced heat and thermally induced melting in granular media. We propose a novel hierarchical multiscale modeling framework, TM-DEMPM, to model the coupled thermo-mechanical behavior in granular media which may undergo large deformation and flow. Material Point Method (MPM) is hierarchically coupled with Discrete Element Method (DEM) to offer physics-based, natural scale-crossing simulations of thermo-mechanical granular responses without assuming complicated phenomenological constitutive models. To offer speedup for the numerical solution, hybrid OpenMP and GPU-based parallelization is proposed to take advantage of the hierarchical computing structure of the framework. The proposed framework may provide an effective and efficient pathway to next-generation simulation of engineering-scale large-deformation problems that involve complicated thermo-mechanical coupling in granular media.

1. Introduction

Granular media are ubiquitous in nature and frequently important to our daily life. A fascinating feature of granular media is their co-existence of solid-like and fluid-like states which may rapidly switch when they are subjected to changes of a variety of factors, including pressure, density, loading and loading rate, saturation ratio, and temperature variation. Importantly, these factors may combine in partial or whole to dictate the behavior of granular media in a complicated coupled manner that is challenging to model and understand. Of particular interest to a wide range of engineering and industrial processes pertaining to granular media is the coupled effect of thermal and mechanical loads, where temperature variation can induce stress and strain changes (i.e., thermally induced stress caused by grain expansion/contraction due to temperature variation) and the mechanical deformation can generate considerable heat in turn (i.e., mechanically induced heat by inter-particle friction dissipation). The thermo-mechanical (TM) coupling effect plays an important role in the engineering and industrial performance of granular media. For example, shakedown matters due to cyclic thermal variation induced stress in thermal energy storage (TES) (Pintaldi et al., 2015) such as the packed-bed TES in concentrated

solar power plants (Becattini et al., 2017) and thermal energy piles in geotechnical engineering (Sani et al., 2019). In addition, deformation and flow processes of granular media may generate considerable heat which in turn influences their physical and/or material properties. Typical examples include the powder-based tabletting process in pharmaceutical manufacturing (Krok et al., 2016) and silo discharging in chemical and mining engineering (Nguyen et al., 2009). A better understanding of the interplay between thermal and mechanical behaviors of granular media could provide crucial theoretical bases for the design, operation, and risk assessment of relevant applications and practices.

The thermo-mechanical coupling not only manifests by direct behavior changes through thermo-mechanical interplay, it also gives rise to changes of thermal and/or mechanical properties of the material or even physical phase changes that may further aggravate the complexity of coupling process. For example, thermally induced melting, as a typical phase transition phenomenon, may occur in cemented granular media such as frozen soils in permafrost areas (Froitzheim et al., 2021) and gas hydrate-bearing soils in submarine settings (Hyodo et al., 2014). Modeling and understanding these typical TM processes becomes critical for design, prediction and assessment of relevant

---

* Corresponding author at: Department of Civil and Environmental Engineering, The Hong Kong University of Science and Technology, Clearwater Bay, Hong Kong SAR, China.

E-mail addresses: ceswzhao@ust.hk (S. Zhao), jzhao@ust.hk (J. Zhao).

geostructures during large deformation and failure of granular media. In agricultural or powder industry, continuous discharging of grains in a silo can accumulate heat to cause remarkable increase of temperature, posing a serious trigger for dangerous silo explosion (Russo et al., 2017). In chemical engineering, impregnation and calcination performance depends crucially on heat transfer and flow properties of granular media in rotary vessels (Saruwatari and Nakamura, 2022). For frozen granular media in nature, the melting process of inter-particle bonds can significantly weaken the strength of granular matrix, triggering large deformation and flow of soils that may cause catastrophic geohazards and environmental disasters (Maslin et al., 2010). For example, the dissociation of gas hydrates in submarine settings may trigger potential geohazards during the course of exploitation, ranging from submarine landslides to earthquakes and tsunamis, threatening the operation and safety of offshore infrastructures and coastal cities (Maslin et al., 2010). Thaw-induced landslides in permafrost areas serve both as an awakening warning of global warming and an exacerbating factor by causing carbon release into the atmosphere (Froitzheim et al., 2021). There are evidently pressing needs from both industrial developments and environmental sustainability to advance our understanding of thermo-mechanical response of granular media, in particular when they reach the regime of large deformation and/or flow.

Great efforts have been devoted to the study of thermo-mechanical coupling in granular media from diversified communities of granular physics, thermal processing industry, and chemical and geotechnical engineering. A prevailing body of these studies have been based on continuum mechanics based models and numerical approaches. They typically smear the discrete nature of a granular material and consider it as a continuum body with homogenized macroscopic responses described by assumed phenomenological constitutive models (Na and Sun, 2017; Liu et al., 2018). To treat an engineering scale boundary value problem, these models are routinely implemented into a continuum-based numerical approach such as Finite Element Method (FEM) and its alternative mesh-free ones such as Material Point Method (MPM) (Sulsky et al., 1995) and Smoothed Particle Hydrodynamics (SPH) (Gingold and Monaghan, 1977) which are specifically useful for large deformation problems (Bui et al., 2008; Lei et al., 2021). Despite their great success, continuum constitutive models may face difficulties in capturing the physical behavior of granular media under complex loading conditions entangled with complicated coupling. When dealing with problems involving large deformation and flow, even greater challenges are posed to both model developments and their implementations. Micromechanics-based approaches and tools, represented by Discrete Element Method (DEM) (Cundall and Strack, 1979), have recently triggered growing interests by their capability of reproducing various complex mechanical characteristics of granular media from a particulate perspective, such as anisotropy and liquefaction (Guo and Zhao, 2013), strain localization and failure (Chen et al., 2011), non-coaxiality (Li and Yu, 2015) and the rich transitional behavior between fluid and solid (Herrmann et al., 2013). Micromechanics approaches can also facilitate the consideration of various coupling processes. Indeed, DEM may accommodate the thermo-mechanical coupling with proper network or pore-scale models (Nguyen et al., 2009; Gan et al., 2012; Choo et al., 2013; Moscardini et al., 2018; Caulk et al., 2020). It can further be coupled with other computational schemes such as Computational Fluid Dynamics (CFD) and Lattice Boltzmann Method (LBM) (Zhang et al., 2016) to simulate coupled hydro-mechanical behavior of granular media. However, computational cost may be an outstanding issue for DEM that limits its practical application for large-scale problems.

Recent spotlights of modeling of granular media have more been attracted by a class of hierarchical multiscale approaches that leverage the strengths of both continuum- and discrete-based methods (Andrade et al., 2011; Chen et al., 2011; Guo and Zhao, 2014; Liu et al., 2016). They employ a hierarchical numerical coupling scheme where DEM is

typically employed to simulate the response of a representative volume element (RVE) as a surrogate of the conventional constitutive model at a material point to feed a continuum-based method, such as FEM (Guo and Zhao, 2014; Liu et al., 2016; Desrues et al., 2019), SPFEM (Guo et al., 2021) and MPM (Liang and Zhao, 2019), for solution of a boundary value problem. The hierarchical coupling structure offered in these approaches enables effective simulations of various engineering problems with complex boundary and initial conditions and yet effortlessly capture the complicated granular material responses that are highly loading path and state dependent. The hierarchical multiscale coupling scheme can be a promising alternative for thermo-mechanical modeling of granular media. Indeed, a hierarchical coupling of FEM and DEM for thermo-mechanical modeling was proposed in our previous study (Zhao et al., 2020), which is, however, limited to thermally induced small deformation and stress regime. It is desirable to develop an alternative multiscale approach that can rigorously tackle TM coupling of granular media in the regime of large deformation and flow.

This work aims at developing an entirely new hierarchical multi-scale framework to simulate coupled thermo-mechanical behavior in large deformation and flow of granular media. The framework will be built upon a pure mechanical hierarchical coupling formulation of MPM and DEM (termed as DEMPM) that was developed for modeling large deformation of granular media (Liu et al., 2017; Liang and Zhao, 2019; Zhao et al., 2021). In DEMPM, a material point serves as an interface for information exchange between the macro-scale MPM solver and the meso-scale DEM solver. Notably, a velocity gradient at a given material point can be obtained first from the MPM solver. It is then passed on to the corresponding RVE assembly as constraints for a DEM solution which is further used to extract required material responses (e.g., stress) to feedback to the MPM solver. The new development incorporating thermo-mechanical coupling will be termed as TM-DEMPM hereafter. To further consider thermo-mechanical coupling in diversified conditions, the generalized interpolation material point method (GIMP) (Bardenhagen and Kober, 2004) will be adopted in TM-DEMPM as the continuum MPM solver to solve both thermal and mechanical fields in a staggered manner at the continuum scale, whereas physics-based thermo-mechanical coupling is fully considered and rigorously modeled at the RVE scale in the DEM solver. As will be demonstrated, the proposed new framework presents three outstanding features when granular media develop deformation en route to large deformation and flow regime: (1) it is able to model thermally induced stress due to grain expansion/contraction; (2) it can capture mechanically induced heat due to inter-particle friction dissipation; and (3) it can handle thermally induced melting at the contact scale. Consequently, TM-DEMPM offers a computational pathway for physics-based, cross-scale modeling and understanding of the thermo-mechanical responses of granular media.

The rest of the paper is organized as follows. Section 2 provides the macroscopic formulation of TM modeling by GIMP, followed by the mesoscopic formulation of TM coupling in DEM in Section 3. Section 4 introduces the hierarchical multiscale coupling and computing scheme. Numerical examples are showcased in Section 5, where the TM-MPM solver is benchmarked against analytical and FEM solutions prior to the validation of TM-DEMPM, followed by three examples representative of typical TM problems in granular media further presented to demonstrate the predictive capabilities and features of the proposed approach, including heat generation in biaxial compression, heat generation in discharge of a granular silo, and melting induced column collapse. Concluding remarks are summarized in Section 6. Tensorial indicial notations and Einstein summation convention are followed in the study, and boldface letters for matrices are used.

2. Thermo-mechanical modeling by GIMP

2.1. Governing equations and weak form formulation

The macroscopic thermo-mechanical response of granular media is modeled in a continuum-based manner, by solving the following

balance equations of energy and linear momentum in an updated Lagrangian framework:

$$\rho c T_{,t} + q_{i,i} = Q_t \tag{1}$$

$$\sigma_{ij,j} + \rho b_i = \rho a_i \tag{2}$$

where ρ is the bulk mass density; c is the specific heat capacity; T is the temperature; t is the time; q_i is the heat flux; Q_t is a heat source or sink; σ_{ij} is the Cauchy stress tensor; b_i is the body force per unit of mass possibly performed on materials (e.g., gravitational acceleration), and a_i is the acceleration term; i, j are sequential indices in $\{1, 2, 3\}$ for 3D or $\{1, 2\}$ for 2D. Note that a latent heat term can be added in Eq. (1) to further consider the effect of phase transition on heat transfer. To avoid unnecessary defocusing of the study, the detailed implementation is not presented in this paper. In future considerations, special attention has to be paid to the different thermal behaviors of coarse and fine soils during phase transition. Notably, the freezing point is widely considered stationary for coarse soils during phase change, whilst it is regarded as a function of temperature for fine soils (Michalowski and Zhu, 2006).

According to the Fourier's law for anisotropic heat conduction, the heat flux q_i can be written as (Onsager, 1931)

$$q_i = -k_{ij} T_{,j} \tag{3}$$

where k_{ij} is the thermal conductivity tensor.

The following general boundary and initial conditions are considered for a typical heat conduction and mechanical problem:

$$T(t) = \bar{T} \quad \text{on} \quad \Gamma_T \tag{4a}$$

$$q(t)_i = \bar{q}_i \quad \text{on} \quad \Gamma_q \tag{4b}$$

$$T(0) = T_{ref} \tag{4c}$$

$$u_i = \bar{u}_i \quad \text{on} \quad \Gamma_u \tag{4d}$$

$$\sigma_{ij} n_j = \bar{t}_i \quad \text{on} \quad \Gamma_t \tag{4e}$$

where Γ_T and Γ_q are the prescribed temperature and heat flux boundaries of the problem domain Ω, respectively; $\bar{T}$ and $\bar{q}_i$ are the prescribed boundary temperature on Γ_T and boundary heat flux on Γ_q, respectively; T_{ref} is the ambient or reference temperature; Eqs. (4a) and (4b) are Dirichlet (fixed temperature) and Neumann (fixed heat flux) boundary conditions, respectively, while Eq. (4c) is the initial condition for temperature distribution at the initial state. n_j is the boundary outward normal of the domain Ω; $\bar{u}_i$ and $\bar{t}_i$ are the prescribed material displacement on Γ_u and boundary traction on Γ_t, respectively; Eqs. (4d) and (4e) are Dirichlet and Neumann boundary conditions, respectively.

Multiplying Eqs. (1) and (2) by a corresponding test function $\omega^{(T)}$ (with zeros on Γ_T) and $\omega_i^{(u)}$ (with zeros on Γ_u), respectively, and integrating over the entire domain Ω by application of integration by parts and Green's formula, the weak form formulations of the governing equations can be obtained as follows

$$\int_\Omega \omega_{,i}^{(T)} k_{ij} T_{,j} d\Omega + \int_\Omega \omega^{(T)} \rho c T_{,t} d\Omega = \int_\Omega \omega^{(T)} Q_t d\Omega - \int_{\Gamma_q} \omega^{(T)} \bar{q} d\Gamma \tag{5}$$

$$\int_\Omega \omega_{i,j}^{(u)} \sigma_{ij} d\Omega + \int_\Omega \omega_i^{(u)} \rho a_i d\Omega = \int_\Omega \omega_i^{(u)} \rho b_i d\Omega + \int_{\Gamma_t} \omega_i^{(u)} \bar{t}_i d\Gamma \tag{6}$$

2.2. Spatial discretization in GIMP

Lagrangian material points and Eulerian background grid are two key ingredients for MPM discretization of a continuum domain. The GIMP formulation was proposed by Bardenhagen and Kober (2004) to overcome the potential cell-crossing issue in the conventional MPM. In the GIMP discretization, the continuum is spatially discretized into a finite set of subdomains occupied by material points with a certain domain for each. The integration over the entire domain Ω governed by the weak forms in Eqs. (5) and (6) can be converted into the summation of integration over each subdomain Ω_p of particles. A

physical field $f(x_i)$ can be obtained by interpolating the corresponding values f_p carried on the material points in terms of the so-called particle characteristic function $\chi_p(x_i)$ (Bardenhagen and Kober, 2004), i.e.,

$$f(x_i) = \sum_p f_p \chi_p(x_i), \tag{7}$$

such that the volume of a material particle is given by

$$V_p = \int_{\Omega_p} \chi_p d\Omega. \tag{8}$$

Note that $\chi_p(x_i)$ satisfies the partition of unity property in the undeformed configuration (Bardenhagen and Kober, 2004) and a "top-hat" function is employed here. For the background grid, a physical field $g(x_i)$ can be also interpolated based on the corresponding value g_I at the grid node I, i.e.,

$$g(x_i) = \sum_I g_I N_I(x_i) \tag{9}$$

where $N_I(x_i)$ is the grid shape function at node I. Note that the subscripts p or I denote properties or functions associated with particle p or node I hereafter.

The weak forms in Eqs. (5) and (6) can be rewritten into the following integration forms over all particles

$$\sum_I \omega_I^{(T)} \sum_J \sum_p m_p c_p \phi_{Ip} N_{Jp} T_{J,t} = \sum_I \omega_I^{(T)} \left[\sum_p V_p \phi_{Ip} Q_{tp} + \sum_p \bar{q}_p h^{-1} \phi_{Ip} \right] + \sum_I \omega_I^{(T)} \sum_p V_p \phi_{Ip,i} k_{pij} T_{p,j} \tag{10}$$

$$\sum_I \omega_I^{(u)} \sum_J \sum_p m_p \phi_{Ip} \phi_J a_{iJ} = \sum_I \omega_I^{(u)} \sum_p m_p \phi_{Ip} b_{ip} + \sum_I \omega_I^{(u)} \sum_p m_p \phi_{Ip} \bar{t}_{ip} h^{-1} - \sum_I \omega_I^{(u)} \sum_p V_p \phi_{Ip,j} \sigma_{pij} \tag{11}$$

where h is the virtual boundary layer thickness serving for the boundary integration (Zhang et al., 2011); m_p is the mass of particle p; ϕ_{Ip} and $\phi_{Ip,i}$ are the weighting and gradient weighting functions, respectively, defined as

$$\phi_{Ip} = \frac{1}{V_p} \int_{\Omega_p} \chi_p N_I d\Omega \tag{12}$$

$$\phi_{Ip,i} = \frac{1}{V_p} \int_{\Omega_p} \chi_p N_{I,i} d\Omega \tag{13}$$

Although several other GIMP variations have been proposed in the literature for better accuracy, e.g., CPDI (Sadeghirad et al., 2011) and CPDI2 (Sadeghirad et al., 2013), the undeformed GIMP (uGIMP) (Bardenhagen and Kober, 2004) is adopted here as the macroscopic solver of the proposed multiscale framework for simplicity in implementation without losing generality.

Due to the arbitrariness of the test functions, the weak forms given by Eqs. (10) and (11) can be simplified into the following semi-discrete equations at node I:

$$\sum_J C_{IJ} T_{J,t} = Q_I^{ext} + Q_I^{int} \tag{14}$$

$$\sum_J M_{IJ} a_{iJ} = f_{iI}^{ext} + f_{iI}^{int} \tag{15}$$

with

$$C_{IJ} = \sum_p m_p c_p \phi_{Ip} N_{Jp} \qquad M_{IJ} = \sum_p m_p \phi_{Ip} \phi_{Jp} \tag{16}$$

$$Q_I^{ext} = \sum_p V_p \phi_{Ip} Q_{tp} + \sum_p \bar{q}_p h^{-1} \phi_{Ip} \qquad Q_I^{int} = \sum_p V_p \phi_{Ip,i} k_{pij} T_{p,j} \tag{17}$$

$$f_{iI}^{ext} = \sum_p m_p \phi_{Ip} b_{ip} + \sum_p m_p \phi_{Ip} \bar{t}_{ip} h^{-1} \qquad f_{iI}^{int} = -\sum_p V_p \phi_{Ip,j} \sigma_{pij} \tag{18}$$

where C and M are the consistent heat capacity matrix and mass matrix, respectively; Q and f_i are heat and mechanical loads, respectively (the superscripts "int" and "ext" denote internal and external loads, respectively). To facilitate the computation, the scheme of lumped matrix is employed, i.e.,

$$C_I = \sum_p m_p c_p \phi_{Ip} \qquad M_I = \sum_p m_p \phi_{Ip} \qquad (19)$$

such that,

$$C_I T_{I,t} = Q_I^{ext} + Q_I^{int} \qquad M_I a_{iI} = f_{iI}^{ext} + f_{iI}^{int} \qquad (20)$$

2.3. Temporal discretization

We employ the Euler forward method to discretize the thermomechanical coupled system (i.e., the semi-discrete equations in Eqs. (20)) in time such that the MPM solver works in an explicit manner. Indeed, this explicit MPM in conjunction with the scheme of lumped matrix has been prevailingly adopted in the literature for its straightforward numerical implementation (de Vaucorbeil et al., 2020). In this scheme, the discrete equations for nodal temperature and velocity are written as:

$$T_I^{(t+\Delta t)} = T_I^{(t)} + T_{I,t}^{(t)} \Delta t \qquad (21)$$

$$v_{iI}^{(t+\Delta t)} = v_{iI}^{(t)} + a_{iI}^{(t)} \Delta t \qquad (22)$$

where the superscripts t and $t + \Delta t$ indicate the variables at the start and end of the processing timestep hereafter, respectively. For the mechanical part, the movement of material points can be solved according to the kinematic fields of the background grid. Two direct candidate methods are considered here, i.e., the so-called FLIP (FLuid Implicit Particle Brackbill and Ruppel, 1986) method and PIC (Particle In Cell Harlow, 1964) method, where particle velocity is updated as

$$v_{ip}^{(t+\Delta t)} = v_{ip}^{(t)} + \sum_I a_{iI}^{(t)} \phi_{Ip}^{(t)} \Delta t \quad \text{for FLIP} \qquad (23)$$

$$v_{ip}^{(t+\Delta t)} = \sum_I v_{iI}^{(t)} \phi_{Ip}^{(t)} + \sum_I a_{iI}^{(t)} \phi_{Ip}^{(t)} \Delta t \quad \text{for PIC} \qquad (24)$$

One major difference between the FLIP and PIC methods is that the FLIP method uses the grid accelerations only while the PIC method uses the updated grid velocities. Stomakhin et al. (2013) suggested a combination of the FLIP and PIC methods by regrading PIC as a damping term as follows:

$$v_{ip}^{(t+\Delta t)} = v_{ip}^{(t)} + \sum_I a_{iI}^{(t)} \phi_{Ip}^{(t)} \Delta t - \alpha_{PIC} \left(v_{ip}^{(t)} - \sum_I v_{iI}^{(t)} \phi_{Ip}^{(t)} \right) \qquad (25)$$

where $\alpha_{PIC} \in [0,1]$ is the PIC fraction. With grid damping α_g and particle damping α_p, the damped particle velocity reads

$$v_{ip}^{(t+\Delta t)} = v_{ip}^{(t)} + \sum_I a_{iI}^{(t)} \phi_{Ip}^{(t)} \Delta t - (\alpha_{PIC} + \alpha_p) v_{ip}^{(t)} + (\alpha_{PIC} - \alpha_g) \sum_I v_{iI}^{(t)} \phi_{Ip}^{(t)} \qquad (26)$$

and the particle position is updated with a general second-order FLIP formulation (Nairn, 2015)

$$x_{ip}^{(t+\Delta t)} = x_{ip}^{(t)} + \sum_I v_{iI}^{(t+\Delta t)} \phi_{Ip}^{(t)} \Delta t$$
$$- \frac{\Delta t}{2} \left(\sum_I a_{iI}^{(t)} \phi_{Ip}^{(t)} \Delta t + (\alpha_{PIC} + \alpha_p) v_{ip}^{(t)} + (\alpha_{PIC} - \alpha_g) \sum_I v_{iI}^{(t)} \phi_{Ip}^{(t)} \right) \qquad (27)$$

Similarly to the FLIP and PIC methods on velocity update in the mechanical part, two possible schemes can be formulated to update the particle temperature, i.e.,

$$T_p^{(t+\Delta t)} = T_p^{(t)} + \sum_I \phi_{Ip}^{(t)} T_{I,t}^{(t)} \Delta t \qquad (28)$$

$$T_p^{(t+\Delta t)} = \sum_I \phi_{Ip}^{(t)} T_I^{(t+\Delta t)} \qquad (29)$$

where the former uses only the incremental temperature of nodes, whereas the latter is a direct remapping of nodal temperatures. The

temperature given by Eq. (29) is the so-called remapped temperature, which is smoother than that given by Eq. (28) (Tao et al., 2016). In this work, the fluctuating particle temperature is tracked to update the nodal temperature, while the smooth particle temperature is taken as an input for the representative volume elements (RVEs). Detail will be introduced in Section 4.

In addition, the timestep should be chosen sufficiently small to maintain numerical stability and convergence in the coupled thermomechanical system. In the proposed staggered coupling algorithm, both the mechanical and thermal solvers adopt the same timestep satisfying the following constrains (Tao et al., 2016; Lei et al., 2021):

$$\Delta t < \frac{l_e}{\sqrt{E/\rho}} \quad \text{for mechanical} \qquad (30)$$

$$\Delta t < \frac{l_e^2 \rho c}{bk} \quad \text{for thermal} \qquad (31)$$

where E is Young's modulus, which can be estimated from odometer tests for an RVE packing (see Section 5.2.2 for detail); b is an adjustable factor, with a default value of 1; l_e is the minimum element size of a mesh; k is the mean thermal conductivity, i.e., average of the diagonal terms of the thermal conductivity tensor k_{ij}.

3. Thermo-mechanical coupling in DEM

3.1. Thermal response of an RVE assembly

3.1.1. Heat generated by friction

Heat can be generated due to friction dissipation at inter-particle contacts during various granular flow processes. Note that heat can be generated through different dissipation processes and mechanisms. Only sliding friction is considered here for simplicity as it has been reported experimentally to dominate the friction dissipation (Zhai et al., 2019). For a single timestep Δt, the total amount of heat within an assembly due to friction dissipation is quantified by

$$E_f = \sum_c f_t^{(c)} v_t^{(c)} \Delta t \qquad (32)$$

where $f_t^{(c)}$ and $v_t^{(c)}$ are friction (tangential force) and relative tangential velocity at contact c during the present timestep. Therefore, the heat source is given by

$$Q = \frac{\sum_{i=1}^N E_f^{(i)}}{V N \Delta t} \qquad (33)$$

where N is the DEM iteration number for a given strain loading; V is the volume of the assembly.

3.1.2. Thermal conductivity tensor

We follow our previous study (Zhao et al., 2020) to construct the fabric-based conductivity tensor for an assembly of non-spherical particles. The derivation is based on such a fundamental assumption that heat flows through an imaginary heat pipe joining the center of each contacted particle (heat reservoir) through the contact (another heat reservoir) as schematically illustrated in Fig. 1(a). Accordingly, a thermal conductivity tensor k_{ij} can be given as

$$k_{ij} = \frac{1}{V} \sum_{p=1}^M \frac{r_i^{(p)} r_j^{(p)}}{\alpha^{(p)} l^{(p)}} \qquad (34)$$

where V is the volume of the assembly; r_i is the vector along the pth heat pipe; l is the branch vector joining the two adjacent particles at the contact of the heat pipe, and α is the thermal resistance per length of the heat pipe.

We note that it is non-trivial to derive an elegant theoretical solution for the thermal conductivity tensor k_{ij} of granular media (Choo et al., 2013). Porosity has been regarded as one of the key factors influencing k_{ij}. The effective thermal conductivity has been frequently assumed to
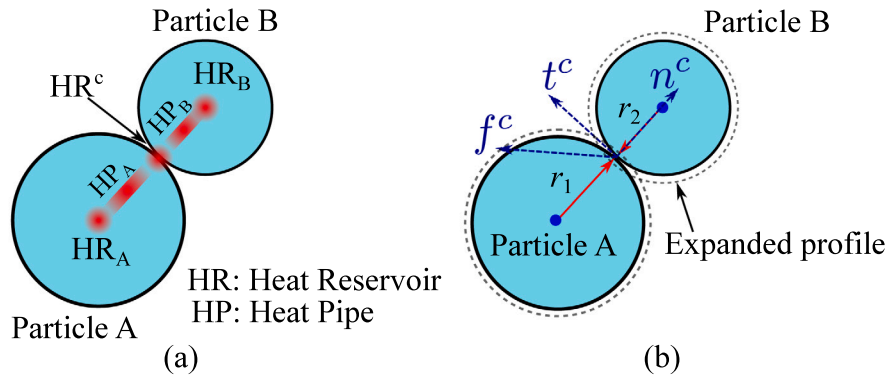
Fig. 1. (a) Heat conduction through an inter-particle contact; (b) thermally induced contact force due to particle expansion.

follow an empirical relation with porosity (Zhang and Wang, 2017), without consideration of the anisotropic nature of materials in an engineering setting, e.g., in geotechnical engineering. Further appraisal is needed to rigorously consider the various physical attributes in deriving a robust expression for effective thermal conductivity of granular media.

Remarks: In the conventional TM modeling with pure DEM, e.g., (Nguyen et al., 2009; Choo et al., 2013), the inter-particle heat transfer has to be modeled at the particle scale for heat flows with remarkable increase in computational cost. By contrast, in the present proposed TM coupling scheme, heat transfer is captured at the mesoscopic/RVE scale (the effect of fabric change can be considered, e.g., on thermal conductivity tensor) and solved in MPM at the continuum scale, which helps to develop the homogenized model with TM coupling and significantly boost the computational efficiency.

3.2. Mechanical response of an RVE assembly

3.2.1. Basic contact model

DEM modeling of granular media commonly postulates a force–displacement law in conjunction with Coulomb's friction condition governing inter-particle contacts (Cundall and Strack, 1979). A simple linear spring contact model is employed here to establish the relation between contact force and relative displacement for each pair of contacting grains as follows

$$f_i^{\,n} = -k_n u_i^n \tag{35a}$$

$$\Delta f_i^{\,t} = -k_t \delta u_i^t \tag{35b}$$

where $f_i^{\,n}$ and $f_i^{\,t}$ are normal and tangential contact forces along the normal n_i^c and the tangential t_i^c directions at contact c, respectively, referring to Fig. 1(b); $\Delta f_i^{\,t}$ is the incremental tangential contact force at the current timestep; k_n and k_t are the normal and tangent contact stiffness, respectively; u_i^n is the penetration depth along contact normal, δu_i^t is the relative tangential displacement of the two contacting particles at the current timestep. The Coulomb condition of friction is applied to constraining the tangential contact force according to,

$$|f^t| \leq \mu |f^n| \tag{36}$$

where μ is the coefficient of friction.

3.2.2. Thermal expansion contact model

For a dry cohesionless granular assembly, the thermally induced stress within an assembly depends on expansion or contraction of particles caused by temperature change. For simplicity, the change of particle size is assumed to be governed by the following relation (Vargas and McCarthy, 2007; Zhao et al., 2017; Zhao and Feng, 2019):

$$R_i = R_i^{(0)}(1 + \beta \Delta T) \tag{37}$$

where $R_i^{(0)}$ is the initial principal length of a particle at the reference temperature; R_i is the current principal length of a particle at a temperature change ΔT with respect to the reference temperature; β is the linear thermal expansion coefficient. As a consequence, the thermally induced change in particle profile yields an additional penetration δd_i, referring to Fig. 1(b).

3.2.3. Thermally sensitive bond contact model

For cemented granular media such as frozen soils in permafrost areas and gas hydrate-bearing soils in submarine settings, particles are bonded together through the ice or ice-like cementation. Such icy bonds are sensitive to temperature change which may cause phase transformation. Such process of inter-particle bonds can be readily considered via proper modification of the contact models (Brown et al., 2014; Shen et al., 2016). For simplicity yet without losing generality, we introduce the following thermally sensitive bond contact model that governs the bond breakage upon heating:

$$F_n > F_{nb}, \quad F_{nb} = \beta_b k_n R \tag{38}$$

$$|F_t| > F_{tb}, \quad F_{tb} = \mu_b F_{nb} \tag{39}$$

where β_b is defined as the breakage strength coefficient with respect to normal contact stiffness k_n; R is the average radius of the two contacting particles; μ_b is a threshold coefficient of the maximum shear force at breakage with respect to the normal breakage force, which is assumed independent of temperature. Once either condition of the above inequalities is met, the bond breaks and can no longer sustain tension. Note that herein we only consider bond breakage subjected to tension and shear, while neglecting bond failure caused by twisting and/or compression. The breakage strength coefficient is a function of temperature T, which can be simply defined as

$$\beta_b = \begin{cases} \dfrac{\beta_a (T_s - T)}{T_s}, & \text{if } T \leq T_s, \\ 0, & \text{otherwise} \end{cases} \tag{40}$$

where β_a is a tuned parameter, and T_s is a threshold for temperature change. Both β_a and T_s are assumed to be constant in the numerical examples in this work. More elegant models will be investigated in our future work.

3.2.4. Periodic cell, deformation and stress

An RVE assembly is assumed to be sufficiently small to capture the response of a material point from the macroscopic perspective and meanwhile sufficiently large to yield a representative response with respect to discrete grains. To reduce the boundary effect from rigid boundaries (e.g., rigid confining walls), periodic boundary conditions are employed in the DEM simulations (Thornton, 2000; Yang et al., 2014; Radjai, 2018). Typically, a parallelepiped-shaped cell is adopted
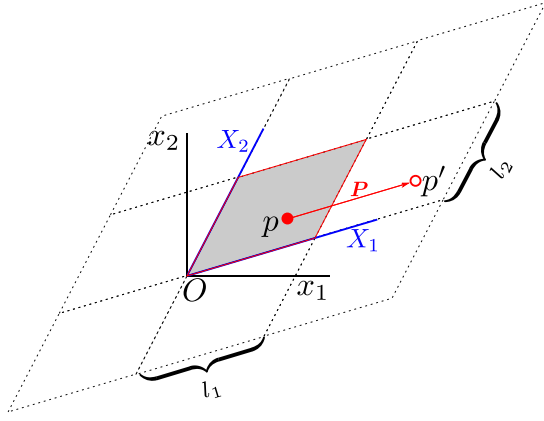
Fig. 2. Two-dimensional illustration of periodic cell ('solid') and its neighbor images ('open-dashed') aligned in a lattice form, after (Zhao et al., 2021).

as the simulation domain of an RVE as shown in Fig. 2, where a parallelogram-shaped RVE cell and its neighbor images are illustrated in 2D. To describe the deformation of an RVE cell, global Cartesian coordinates (x_i) and local oblique Cartesian coordinates (X_i) are introduced, which are also known as Eulerian (spatial) and Lagrangian (material) coordinates in continuum mechanics, respectively.

A deformation (gradient) tensor H_{ij} can be introduced to convert material position between the global and local coordinates, such that

$$x_i = H_{ij}X_j \tag{41a}$$

$$X_j = H_{jk}^{-1}x_k \tag{41b}$$

where H_{ij} has columns as the basis vectors of the cell, while H_{ij}^{-1} is for the inverse transformation. The material time derivative for Eq. (41a) reads

$$\dot{x}_i = \underbrace{\dot{H}_{ij}X_j}_{v_{hi}} + \underbrace{H_{ij}\dot{X}_j}_{v_{fi}} \tag{42}$$

where v_{hi} is the affine mean-field velocity due to the macroscopic homogeneous deformation of the RVE cell; v_{fi} is the non-affine velocity or fluctuating velocity, i.e., particle velocity driven by the resultant force on the particle.

Given a particle p in the RVE cell, its position may change to p' outside the RVE cell. With the periodic boundary condition that particles move and periodically cross the boundaries (cell bases) to stay within the cell, the image p' in other cells can be periodically shifted back to the RVE cell in the local coordinate system by

$$X_i(p') = X_i(p) + P_i \tag{43}$$

with

$$P_i = p_{ij}l_j \tag{44a}$$

$$p_{ij} = \begin{cases} \lfloor \frac{X_i(p')}{l_j} \rfloor, & \text{if } i = j, \\ 0, & \text{otherwise} \end{cases} \tag{44b}$$

where P_i is the periodic (shifted) vector; p_{ij} is a diagonal matrix with period number for the corresponding axis as the diagonal; l_j is the base length of the cell along X_j, as shown in Fig. 2; $\lfloor * \rfloor$ denotes rounding down to the nearest integer. With Eq. (43), the mean-field velocity $v_{hi}(p')$ and the fluctuating velocity $v_{fi}(p')$ at the image p' of a particle p can be written as

$$v_{hi}(p') = v_{hi}(p) + \dot{H}_{ij}P_j \tag{45a}$$

$$v_{fi}(p') = v_{fi}(p) \tag{45b}$$

which suggests that the mean-field velocity v_{hi} is non-periodic while the fluctuating velocity v_{fi} is periodic in the presence of periodic boundary conditions.

The additional velocity arisen from the homogeneous deformation of the RVE cell is obtained in the global coordinate system:

$$v_{hi} = L_{ij}x_j \tag{46a}$$

$$L_{ij} = \dot{H}_{ik}H_{kj}^{-1} \tag{46b}$$

where L_{ij} is the velocity gradient tensor of the cell deformation.

In the present proposed framework, an RVE is subjected to small deformation increments through strain-controlled loading during each DEM step. The strain tensor ϵ_{ij} of the periodic cell (RVE) is taken to measure the homogenized deformation of the assembly, i.e.,

$$\epsilon_{ij} = \frac{1}{2}(H'_{ij} + H'_{ji}) - \delta_{ij} \tag{47}$$

where H'_{ij} is the deformation gradient tensor with respect to the reference configuration. The volumetric strain ϵ_v and the deviatoric strain ϵ_q are given by

$$\epsilon_v = \epsilon_{ii} \tag{48a}$$

$$\epsilon_q = \sqrt{\frac{2}{3^{n-2}}\epsilon'_{ij}\epsilon'_{ij}} \tag{48b}$$

in which ϵ'_{ij} is the deviatoric strain tensor, $\epsilon'_{ij} = \epsilon_{ij} - \frac{1}{n}\epsilon_v\delta_{ij}$; $n = 2$ or 3 for 2D or 3D, respectively. Note that for strain-controlled loading at each DEM step, the velocity gradient L_{ij} is prescribed.

The homogenized stress tensor σ_{ij} within an RVE assembly can be expressed from contact forces and fluctuating velocities of particles (Christoffersen et al., 1981; Radjai, 2018), i.e.,

$$\sigma_{ij} = \frac{1}{V}\sum_{c\in V}f_i^c b_j^c + \frac{1}{V}\sum_{p\in V}m_p v_{fi}^p v_{fj}^p \tag{49}$$

where V is the volume of the assembly; f_i^c and b_j^c are the contact force and the branch vector, respectively; m_p is the mass of particle p. It is worth noting that the contact force-related term denotes stress transmission through contact force networks, whereas the fluctuating velocity-related term reflects the kinetic stress associated to the momenta transferred by particles.

4. Multiscale coupling and computing scheme

4.1. Macro–micro bridging and coupling

In conventional thermo-mechanical coupling studies, thermally-dependent constitutive models are commonly employed to capture the thermo-mechanical response of granular media (e.g., soils) from a phenomenological perspective. It is typical to consider thermally induced expansion/contraction in the deformation of a continuum exposed to temperature change, such that the thermally induced stress can be taken into account in terms of the following stress–strain relation,

$$\dot{\sigma} = D : \dot{\epsilon} \tag{50}$$

$$\dot{\epsilon} = \frac{1}{2}[L + L^T] - \beta\dot{T}I \tag{51}$$

where $\dot{\sigma}$ and $\dot{\epsilon}$ are rate tensors of stress and strain, respectively; D is a fourth-order material tensor; $\dot{T}$ is the rate of temperature change; β is the linear thermal expansion coefficient; I is the unit tensor.

The hierarchical multiscale modeling framework (Guo and Zhao, 2014; Liang and Zhao, 2019; Zhao et al., 2020) provides an ideal setting to couple the thermo-mechanical responses at the particulate scale in a seamless and physical manner. Indeed, DEM-simulated RVEs can be introduced to bridge the macroscopic and microscopic thermo-mechanical responses for a granular medium. At the macroscopic scale, both deformation and temperature can be obtained by solving the
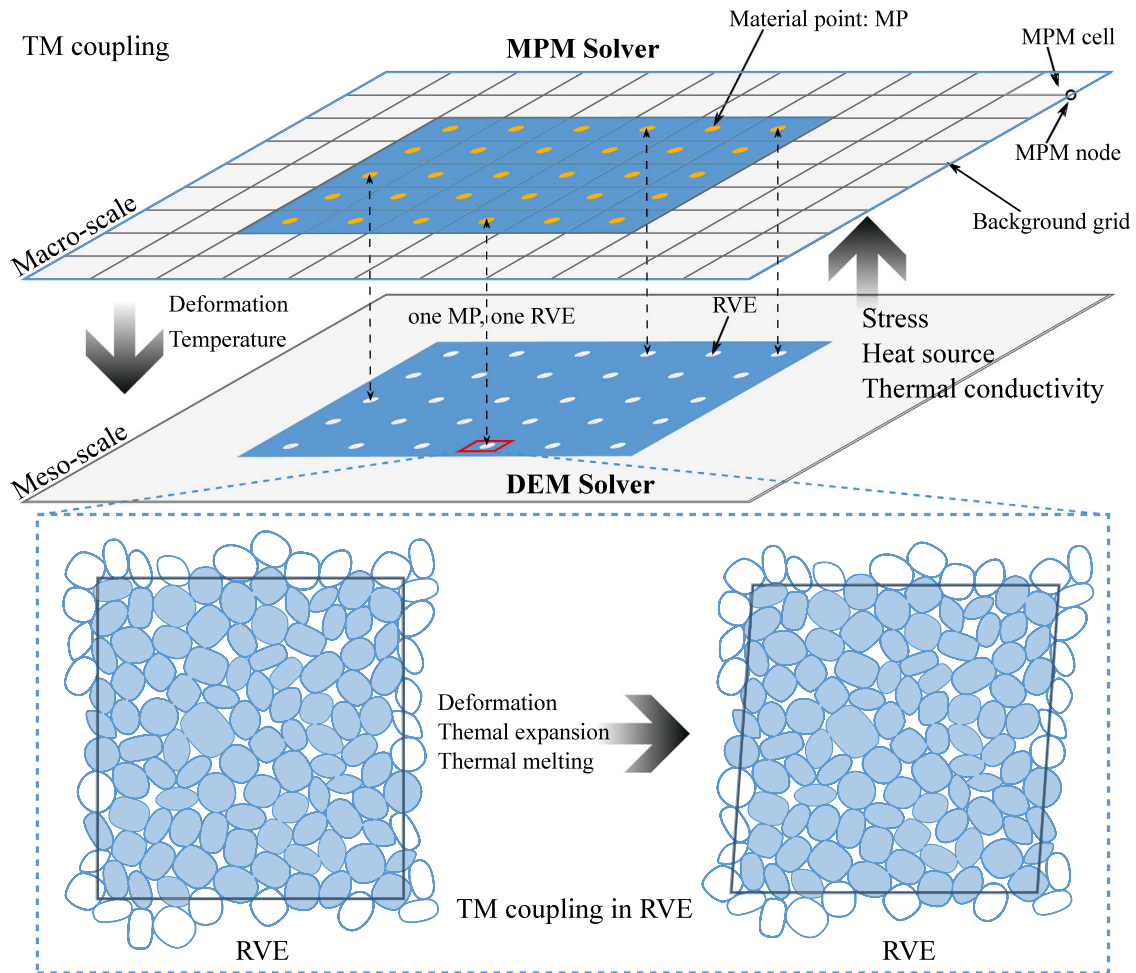
Fig. 3. Illustration of the solution procedure for hierarchical multiscale modeling of thermo-mechanical response in granular media.

corresponding boundary and initial value problems with a continuum-based numerical method, e.g., MPM in this work. Out of the solution, the deformation (strain and its rate) and temperature can be extracted for each material point and are passed onto the attached RVE assembly as boundary conditions. Subjected to the imposed boundary conditions of deformation and temperature, DEM computation is performed for each RVE to find the thermo-mechanical response for the material point at the constrained state which are returned to the material point to advance the continuum solution. Note that in such a hierarchical multiscale modeling scheme, the DEM solver may run explicitly with a different timestep Δt^{DEM} than that of the MPM solver. Nevertheless, it is suggested to take the same timestep for the heat generation problems to be treated here.

4.2. Solution procedure

Fig. 3 illustrates the computation procedure of the proposed hierarchical TM-DEMPM framework. The major solution steps are summarized as follows:

(1) Establishing a simulation domain with material points and a background grid, and attaching an RVE assembly to each material point;
(2) Computing shape functions $\phi_{Ip}, \phi_{Ip,i}$ for each material point, and mapping particle mass, momentum and temperature to nodes;

(3) Applying deformation gradient and temperature to the attached RVE, then running DEM simulations for RVEs to obtain corresponding stress and heat source, and updating temperature gradient and heat flux;
(4) Computing nodal force, temperature load (heat load), and updating nodal temperature;
(5) Updating particle momentum and position, remapping temperature, and going back to Step (2) for the next timestep.

4.3. Hybrid OpenMP and GPU-based parallelization

Between the MPM and DEM solvers in the proposed TM framework, the DEM solver is much more computationally intensive than the MPM one. To tackle the challenge, a hybrid OpenMP and GPU-based parallelization is proposed with pseudocode listed in Algorithm 1. For the MPM solver, each for-loop is parallelized with OpenMP, whereas a thread-block-wise approach (Zhao et al., 2021) is employed to accelerate RVE DEM simulations on GPUs. Note that the MPM solver can be readily enhanced on GPUs for further acceleration (Dong et al., 2015), which is, however, beyond the scope of this work.

5. Numerical examples

The TM-MPM is first benchmarked against analytical and FEM solutions for one- and two-dimensional transient problems of thermoelastic materials in Section 5.1, followed by the validation of the TM-DEMPM

Algorithm 1: Pseudocode of the proposed TM-DEMPM framework.

1 Discretizing the domain and attaching RVEs;
2 **foreach** *timestep* **do**
3   **foreach** *node I {OpenMP acceleration}* **do**
4   Cleaning all physics quantities such as mass, momentum, temperature, etc;
5   **foreach** *material point p {OpenMP acceleration}* **do**
6   **foreach** *neighbor node I* **do**
7   Computing shape function;
8   Setting general boundary conditions;
9   **foreach** *node I {OpenMP acceleration}* **do**
10   Mapping particle mass, momentum and temperature to nodes;
11   **foreach** *material point p {OpenMP acceleration}* **do**
12   Obtaining deformation gradient and temperature;
13   **foreach** *block i in the Grid of Blocks of threads {GPU acceleration}* **do**
14   **if** $i < N_p$ **then**
15   Applying deformation gradient and temperature;
16   Running the RVE DEM simulation on Block *i*;
17   **foreach** *material point p {OpenMP acceleration}* **do**
18   Obtaining stress and heat source;
19   Updating temperature gradient and heat flux;
20   Applying traction boundary condition;
21   **foreach** *node I {OpenMP acceleration}* **do**
22   Computing nodal force, heat load, and updating nodal temperature;
23   **foreach** *material point p {OpenMP acceleration}* **do**
24   Updating momentum and position, remapping temperature;

Fig. 4. MPM model of the semi-infinite bar with a point A of interest.

implementation for one- and two-dimensional thermo-mechanical coupling problems in Section 5.2. Three examples representative of typical thermo-mechanical problems in granular media are further presented to demonstrate the predictive capabilities and features of the proposed approach, including heat generation in biaxial compression tests, heat generation in discharge of a granular silo, and melting induced column collapse in Section 5.3.

5.1. Benchmarks of the TM-MPM

5.1.1. Transient TM response of a semi-infinite bar

We consider a half-space infinite thermoelastic body subjected to transient heat transfer (or the so-called Danilovskaya Problem) (Danilouskaya, 1950). It can be simplified into a one-dimensional bar when the entire free surface is exposed to a uniform ambient temperature. Such a semi-infinite bar with an initial temperature of T_0, shown in Fig. 4, is subjected to heating at a constant temperature T_1 at its free end (i.e., $T(0, t) = T_1$). The evolution of temperature at any point x is given by

$$T(x, t) = erfc\left(\frac{x}{2\sqrt{\alpha t}}\right)(T_1 - T_0) + T_0 \tag{52}$$

with

$$erfc(x) = 1 - \frac{2}{\sqrt{\pi}} \int_0^x e^{-\eta^2} d\eta \tag{53}$$

where $erfc(x)$ is the complementary error function.

The simulation setup is depicted in Fig. 4. The semi-infinite bar is modeled as a finite length of $L = 6$ m in MPM, which is discretized
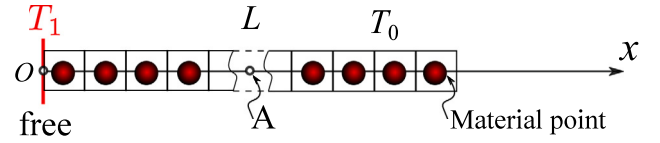
into 300 quadrilateral cells with one material point for each. The initial temperature T_0 and heating temperature T_1 are set to 0 and 100 °C, respectively. For the sake of convenience, the material parameters such as material density ρ, specific heat capacity c, Young's modulus E and thermal conductivity coefficient k are all set to be unit, while the Poisson's ratio ν and linear thermal expansion coefficient β are set to be 0 and 1×10^{-6}/°C, respectively. No grid and particle damping is introduced, while the PIC fraction α_{PIC} is set to a small number, i.e., 0.0001 here. The simulation runs 3 s in total with a fixed timestep of 1×10^{-4} s.

Fig. 5 shows the evolution of temperature, normal stress and displacement at point A ($x = 1$ m). The normal stress σ_x and displacement u_x are normalized to be dimensionless as u and σ, respectively, to ease the deduction of the analytical solutions for comparison (Balla, 1991). The predicted temperature is found to be consistent with the analytical solution in Eq. (52). Applying the assumed material properties, the dimensionless normal stress σ and dimensionless displacement u at Point A read

$$\sigma = \sigma_x/(\beta T_1), \quad u = u_x/(\beta T_1) \tag{54}$$

As shown in Fig. 5, the simulated dimensionless normal stress σ and dimensionless displacement u are in a good agreement with the analytical results. As reported in Tao et al. (2016), certain oscillations are found in the simulated σ due to spurious noises introduced by the full FLIP scheme in Fig. 5(b), which can be mitigated by advanced techniques including XPIC (Hammerquist and Nairn, 2017). Overall, the numerical realization has been well implemented for the TM coupling in MPM overall.

5.1.2. Transient TM response of a 2D plate

We consider a 1 m-by-1 m square plate with an initial temperature of $T_0 = 0$ °C. Its x-displacement at the left boundary and y-displacement at the bottom boundary are fixed, while the other two boundaries are free. The plate is assumed to be an isotropic, linearly thermo-elastic material, with material density $\rho = 1$ kg/m^3, specific heat capacity $c = 1$ J/(kg K), Young's modulus $E = 1$ Pa, thermal conductivity coefficient $k = 0.1$ W/(m K), Poisson's ratio $\nu = 0.25$, and linear thermal expansion coefficient $\beta = 1 \times 10^{-6}$/°C. The plate is subjected to a sudden heating at both the left and bottom boundaries with a constant temperature $T_1 = 1$ °C. For the present transient problem, it is non-trivial to obtain the analytical solution of the coupled TM responses. Thus, a commercial FEM solver Abaqus/Explicit has been employed to prepare the benchmarked results. The domain is discretized into 40×40 elements or cells for FEM and MPM, respectively, as shown in Fig. 6(a). Each cell has a single material point in MPM, corresponding to a quadrilateral element with reduce integration for FEM. The dynamic simulations run for 0.5 s with a fixed timestep of 1×10^{-3} s. Note that no damping is introduced in either simulation. Figs. 6(b) and (c) show the temperature contours from MPM and FEM simulations at $t = 0.5$ s. Evidently, the prediction of temperature distribution made by MPM is consistent with that by FEM.

Fig. 7 presents a further quantitative comparison of the evolutions of temperature and stress for three monitored points in the plate as shown in Fig. 6(a): A at the plate center with $x = y = 0$ m, B at (0.1, 0) m, and C at (0.1, 0.1) m. As is shown, the MPM predictions are in good agreement with the FEM simulation. The two benchmark
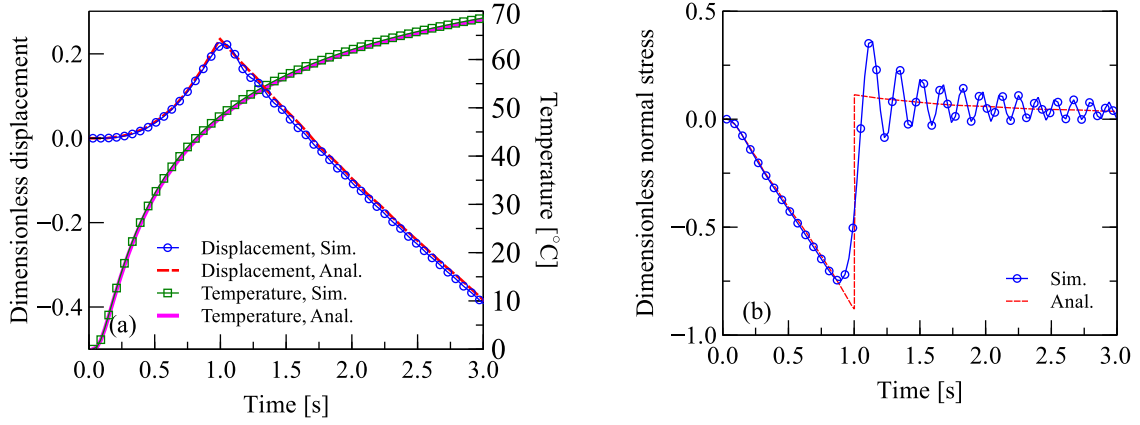
Fig. 5. (a) Dimensionless displacement and temperature, (b) Dimensionless normal stress at $x = 1$ m.
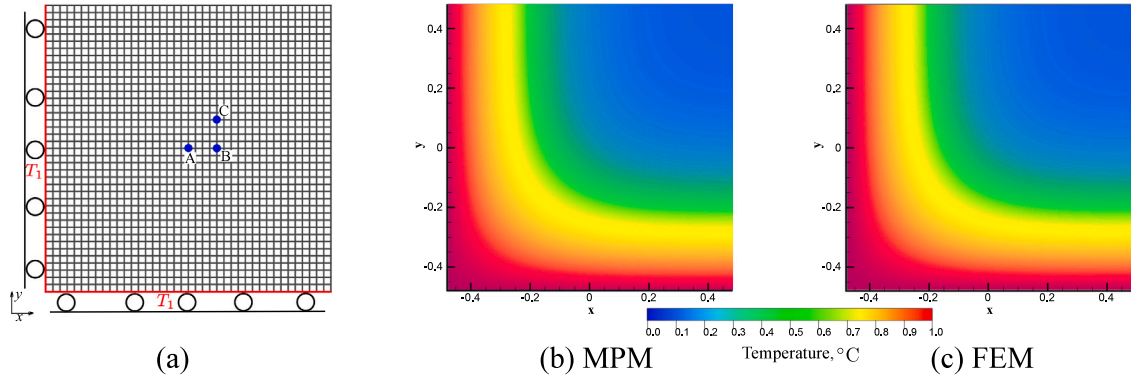

Fig. 6. (a) Mesh and boundary conditions; temperature distributions simulated by MPM (b) and FEM (c) at $t = 0.5$ s.

examples indicate the TM coupling has been correctly implemented in the proposed GIMP scheme.

5.2. Verification of the TM-DEMPM

5.2.1. One dimensional heat conduction

To validate the integrated coupled TM-DEMPM framework, we first consider a rod fixed at both ends with a length of $L = 1$ m and initial temperature T_0, as shown in Fig. 8(a). It is subjected to a sudden heating at the right end ($x = L$) while maintaining a reference temperature at the left end ($x = 0$), i.e., $T_1 = T_0 = 0$ °C and $T_2 = 100$ °C. The transient temperature across the rod can be obtained analytically by the following:

$$T(x,t) = T_0 + (T_1 - T_0)\frac{x}{L} + \frac{2(T_1 - T_0)}{\pi}\sum_{n=1}^{\infty}\frac{(-1)^n}{n}e^{-(\frac{n\pi}{L})^2\frac{kt}{\rho c}}\sin(\frac{n\pi x}{L}) \quad (55)$$

To facilitate the theoretical derivation, the thermo-mechanical response of the rod is assumed to be quasi-statically coupled. The thermally induced axial stress $\sigma_x(x,t)$ and displacement $u(x,t)$ across the rod can be analytically obtained in the following approximate integration:

$$\sigma_x(x,t) = -K\frac{1}{L}\int_0^L \beta T(x,t)\mathrm{d}x$$
$$= -\frac{T_1 + T_0}{2}K\beta + \frac{4K\beta(T_1 - T_0)}{\pi^2}\sum_{n=0}^{\infty}\frac{1}{(2n+1)^2}e^{-\frac{(2n+1)^2\pi^2}{L^2}\frac{kt}{\rho c}} \quad (56)$$

$$u(x,t) = \beta\int_0^x T(x,t)\mathrm{d}x - \frac{\beta x}{L}\int_0^L T(x,t)\mathrm{d}x$$
$$= \frac{\beta x(T_1 - T_0)}{2L}(x - L) - \frac{2\beta L(T_1 - T_0)}{\pi^2}\times \quad (57)$$
$$\sum_{n=1}^{\infty}\frac{(-1)^n}{n^2}e^{-(\frac{n\pi}{L})^2\frac{kt}{\rho c}}(\cos\frac{n\pi x}{x} - \frac{x}{L}\cos(n\pi) + \frac{x}{L} - 1)$$

where β is the linear thermal expansion coefficient; K is the axial stiffness of the rod which can be estimated from the first component of the stiffness matrix $D_{\alpha\beta\gamma\phi}$. By assuming uniform deformation, the averaged stiffness tensor can be obtained by partial derivative of the stress tensor with respect to the deformation as (Wren and Borja, 1997; Luding, 2004)

$$D_{\alpha\beta\gamma\phi} = \frac{1}{V}\sum_{c\in V}(k_n n_\alpha^c l_\beta^c n_\gamma^c l_\phi^c + k_t t_\alpha^c l_\beta^c t_\gamma^c l_\phi^c) \quad (58)$$

where k_n^c and k_t^c are the normal and tangential contact stiffness at contact c, respectively.

As shown in Fig. 8(b), the rod is uniformly discretized into 50 cells with single material point for each. A constant confining stress σ_0 of 100 kPa is applied to both the upper and lower boundaries. Simulations are conducted using both TM-DEMPM approach and TM-MPM for the purpose of comparison. For the TM-DEMPM, identical RVE packings after isotropic consolidation with a confining stress of 100 kPa are attached to each material point of the MPM. The detail on the consolidation of the RVE packing is not presented here for brevity. Interested readers are referred to the conventional procedures for DEM simulations in the literature, e.g., (Zhao et al., 2018). As the focus is placed on the response along the bar, a regular packing of 400 mono-sized disks (with radius $r = 5$ mm), as shown in Fig. 8(c), is employed to maintain a constant fabric during loading, thereby ensuring an almost invariant bulk Young's modulus for a better comparison with the analytical solutions. Note that 400 particles are adequate to yield homogeneous response of a 2D RVE as reported in the previous study (Guo and Zhao, 2014), and particle number is thus set to 400 for all RVEs at the rest simulations through this work. Moreover, following our previous study (Zhao et al., 2020), a fictitious third dimension $z_p = 75$ mm for the 2D RVE packing is introduced to calculate the RVE volume involved in the computation
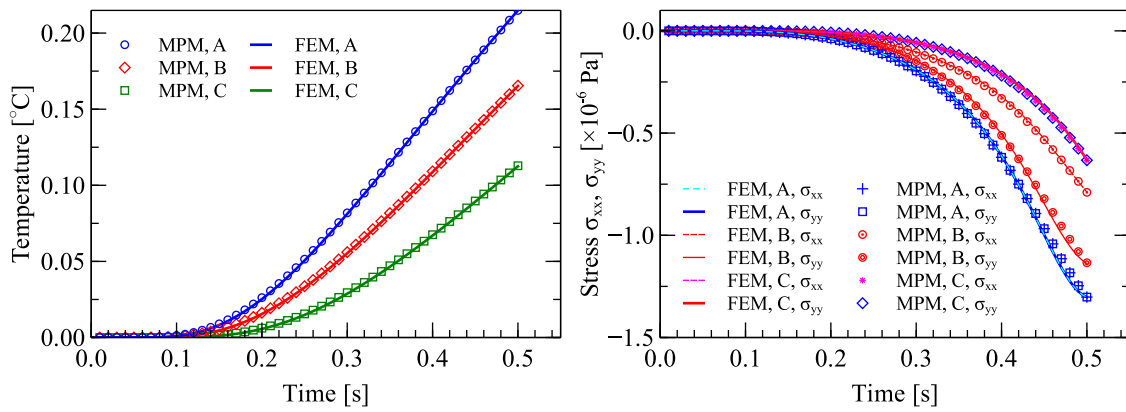
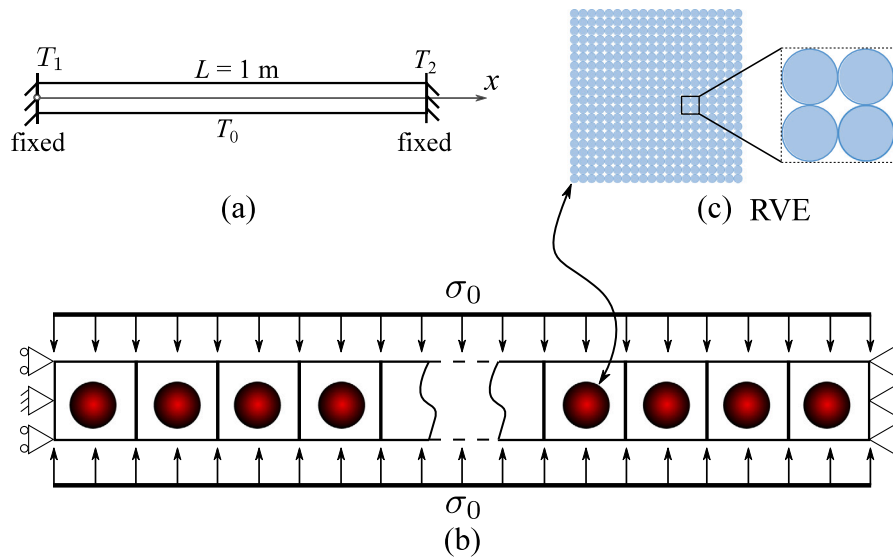**Fig. 7.** (a) Temperature, (b) stress at three different points A, B and C.

Fig. 8. (a) A simplified granular rod; (b) Cells and boundary conditions; (c) Material-point assigned RVE with regular packing of disks.

Table 1
Material properties for TM-MPM and TM-DEMPM simulations.

Parameter	TM-DEMPM	TM-MPM
Material density ρ, kg/m^3	2650	2650
Specific heat capacity c, J/(kg K)	1/2650	1/2650
Young's modulus E, Pa	–	1.33×10^7
Thermal conductivity coefficient k, W/(m K)	0.1	0.1
Poisson's ratio v	–	0
Linear thermal expansion coefficient β, /$^\circ$C	1×10^{-4}	1×10^{-4}
Inter-particle contact stiffness k_n, k_t, N/m	1×10^6	–
Inter-particle coefficient of friction μ	0.001	–

of stress. The material properties are selected from the literature for both DEMPM and pure MPM simulations, listed in Table 1, which will be used in all remaining simulations of the study unless otherwise stated. Note that the gravitational force is not considered in the quasi-static simulations due to negligible inertia effects. The particles are assumed almost frictionless to ensure relatively small deviations in the material properties (e.g., Young's modulus) among all RVEs during the simulation, thereby rendering it reasonable to use constant material properties in the analytical solutions. Both simulations run 1.0 s with a fixed timestep of 1×10^{-4} s.

Fig. 9 shows the evolutions of temperature, axial stress and displacement across the rod from the TM-MPM and TM-DEMPM simulations. As shown in Fig. 9(a) and (d), the temperature from the simulated results

are evidently consistent with the analytical ones for both TM-MPM and TM-DEMPM cases. For the axial stress and displacement, slight deviations between the simulated and analytical results are observed. Note that the analytical solution has been derived based on the assumption of a quasi-static condition (it is non-trivial to derive transient solutions), while the simulations have been conducted under transient conditions. Interestingly, it is observable that a stress wave propagates across the rod and relaxes with time (see Fig. 9(b) and (e)). Moreover, the simulated axial stress is in a good agreement with the analytical one after 0.4 s for both TM-MPM and TM-DEMPM, suggesting the rod has reached a quasi-static equilibrium. As for the displacement in Fig. 9(c) and (f), the simulated and analytical results match reasonably well with each other, in consideration of the possible discrepancy between the analytical (quasi-static) and exactly transient solutions.

5.2.2. Two-dimensional heat conduction

We further consider a two-dimensional square specimen composed of dense discrete particles with an initial temperature of $T_0 = 0$ °C. All its boundaries (length of $L = 1$ m for each) are exposed to heat source with a constant temperature of $T_1 = 100$ °C. The normal displacement of all boundaries is fixed. The entire domain is discretized into 40×40 cells with single material point for each, as shown in Fig. 10(a). The RVE attached to each material point is identical and consists of 400 disks with radii uniformly ranging between [0.25, 0.5] mm. The other DEM parameters are adopted the same as for the example in
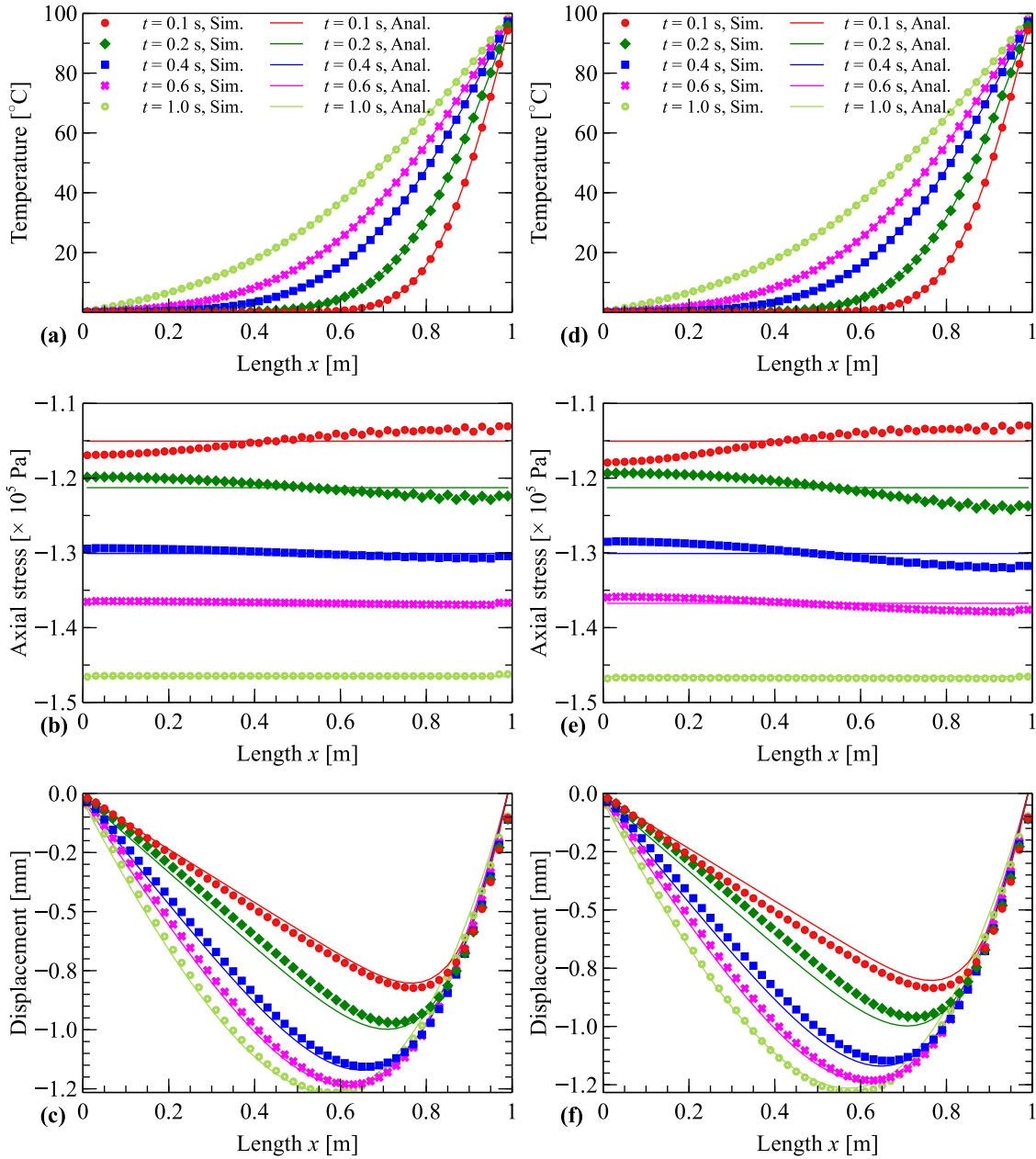
Fig. 9. Evolution of temperature, axial stress and displacement across the rod simulated from the TM-MPM (a–c, left) and the TM-DEMPM (d–f, right).

Section 5.2.1. The RVE packing is consolidated to a confining stress of 100 kPa. The corresponding configuration and contact force network at the end of consolidation are shown in Fig. 10(b). For the present problem, the analytical temperature at a point (x, y) of the plate is given as (Tao et al., 2016)

$$T(x, y, t) = T_1 - \frac{16(T_1 - T_0)}{\pi^2} \sum_{m=0}^{\infty} \sum_{n=0}^{\infty} \frac{e^{-\frac{\pi^2(m^2+n^2)}{L^2} \frac{kt}{\rho c}}}{(2m+1)(2n+1)}$$
$$\times \sin \frac{(2m+1)\pi x}{L} \sin \frac{(2n+1)\pi y}{L} \tag{59}$$

where x and y are Cartesian coordinates with the origin in the lower-left corner of the specimen.

To render a reasonable comparison between the TM-MPM and TM-DEMPM results, the elastic properties in TM-MPM are estimated based on a uniaxial compression test of the RVE packing. Fig. 10(c) shows the increments of both stress and strain during the compression of a single RVE packing, where almost linear stress–strain relations can be

obtained for small-strain response of the RVE: $\Delta\sigma_{yy}/\Delta\epsilon_{yy} = K + G \approx$ 12.4 MPa and $\Delta\sigma_{xx}/\Delta\epsilon_{yy} = K - G \approx 2.18$ MPa. Therefore, the Poisson's ratio v and Young's modulus E can be estimated as $v = (K-G)/(K+G) \approx$ 0.18 and $E = 2K(1-v) \approx 12.00$ MPa, respectively, in 2D (Meille and Garboczi, 2001). They are then introduced as the inputs for the TM-MPM simulations.

Fig. 11 shows the evolutions of temperature and stress at Point A from both the TM-MPM and TM-DEMPM simulations. It can be seen that both simulated temperatures match well with the analytical solution. For the stress, it is not surprising that σ_{xx} and σ_{yy} are identical in the TM-MPM simulation due to the symmetry of the problem. By contrast, σ_{xx} shows a slight deviation from σ_{yy} for the TM-DEMPM simulation, which is attributed to the intrinsic anisotropy of granular assembly for the RVE. Meanwhile, the bulk modulus of granular media is loading-dependent such that the TM-DEMPM results differ slightly from that of the TM-MPM simulation. Detailed discussion on the response of granular media is beyond the scope of this work.
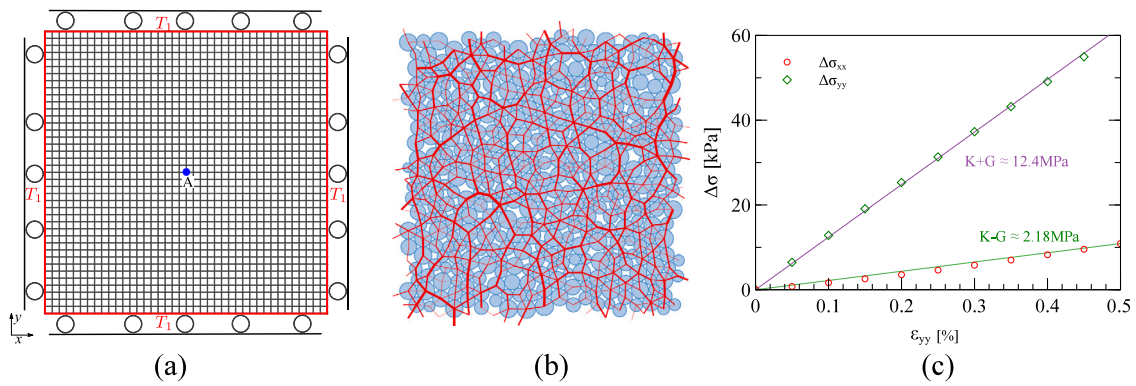
Fig. 10. (a) Mesh and boundary conditions, (b) an RVE packing with an isotropic stress of 100 kPa (the red segments denote the contact force network), and (c) stress increment $\Delta\sigma$ with loading strain ϵ_{yy} for uniaxial compression test on the RVE packing.
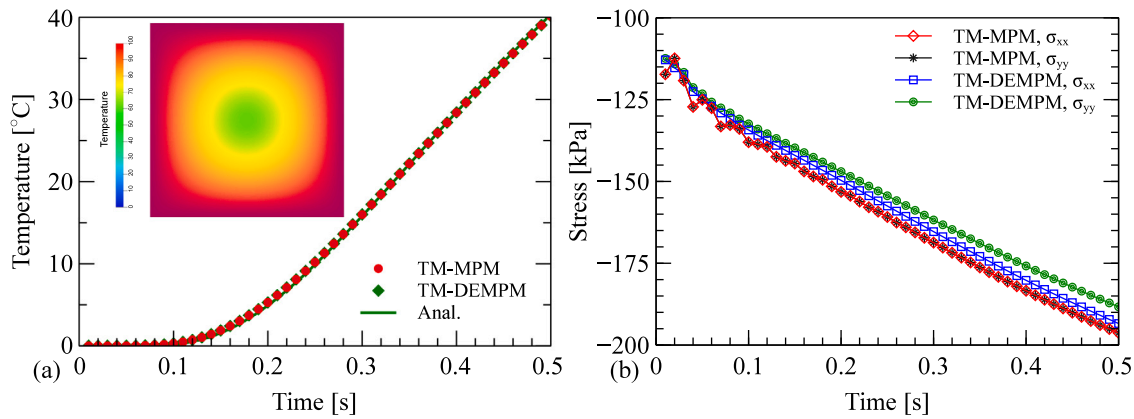

Fig. 11. Evolution of (a) temperature (the inset denotes the contour at $t = 0.5$ s) and (b) stress (σ_{xx}, σ_{yy}) at the plate center simulated from TM-MPM and TM-DEMPM.

5.3. Simulations of typical thermo-mechanical problems

5.3.1. Heat generation in biaxial compression

Three typical thermo-mechanical coupling problems of engineering relevance are chosen to showcase the predictive capability of our proposed TM-DEMPM. Considered first is a simulation of biaxial compression tests on two 1 m-by-2 m specimens with dense and loose initial states, respectively. Fig. 12(a) illustrates the simulation setup wherein a confining stress of $\sigma_{xx} = 100$ kPa is applied at both lateral sides, and the loading plates of the specimen are assumed to be rough. The domain of the specimen is discretized into 10×20 square cells with 4 material points for each cell. The same protocol of RVE packing generation in Section 5.2.2 is used to prepare different RVE packings by setting different inter-particle coefficients of friction μ during the consolidation to obtain dense and loose specimens. Two RVE packings with a void ratio (i.e., void volume over solid volume) of 0.165 (dense) and 0.236 (loose), respectively, are prepared by setting $\mu = 0.01$ and $\mu = 0.5$, respectively. Snapshots of the two RVE packings aggregated with contact force network at the end of consolidation are shown in Figs. 12(b) and (c). The coefficient of friction μ is set to 0.5 prior to shearing for both specimens. The other material parameters are the same as in Section 5.2.2 except for the following: thermal resistance 1×10^3 K/(W m) for an initial thermal conductivity of 1.6 W/(m K), and specific heat capacity 670 J/(kg K) for quartz (Zhao et al., 2020).

The simulation adopts a timestep of 0.001 s. The loading plate is pushed downwards with a constant velocity of 0.02 m/s. The simulation is terminated when a target loading strain $\epsilon_{yy} = 20.0\%$ is attained. Fig. 13 shows the evolution of the vertical reaction stress σ_{yy} on the loading plate for both dense and loose specimens during the compression. The dense and loose specimens are found to experience softening and hardening responses during the shearing, respectively, before reaching relatively stable values, which is consistent with the laboratory observation on sands.

Fig. 14 records the progressive deformation of the specimen at four different loading strain levels, where both volume (specimen profile) variation and shear band are reproduced qualitatively against the well-known experimental observation, e.g., in Evans and Frost (2010). In particular, the shear band identified by deviatoric strain ϵ_q shows the dense specimen is sheared more intensively within the shear band than the loose one at the same level of loading strain. Moreover, the shearing also triggers an apparent friction dissipation, as evidenced by the higher temperature profile in the shear zone. Interestingly, it can be seen that the region experienced noticeable temperature increase is slightly larger than the shear zone, probably due to heat diffusion. Luong (2007) measured temperature increase due to friction dissipation within silica sands under cyclic loading in triaxial tests using infrared thermography, where the temperature increase amounts up to 5 °C at a similar level of stress as this work. Compared with the experimental measure, our simulated temperature increase of up to 1.6 °C is quantitatively reasonable. Overall, the proposed framework provides an alternative pathway for simulating thermal evolution and its interaction with mechanical response within granular materials involving large deformation, e.g., pharmaceutical powder tabletting (Krok et al., 2016) where temperature matters during mechanical handling.

5.3.2. Heat generation in discharge of a granular silo

Temperature increase has been well observed in granular materials discharging out of a silo. The discharge of a granular material
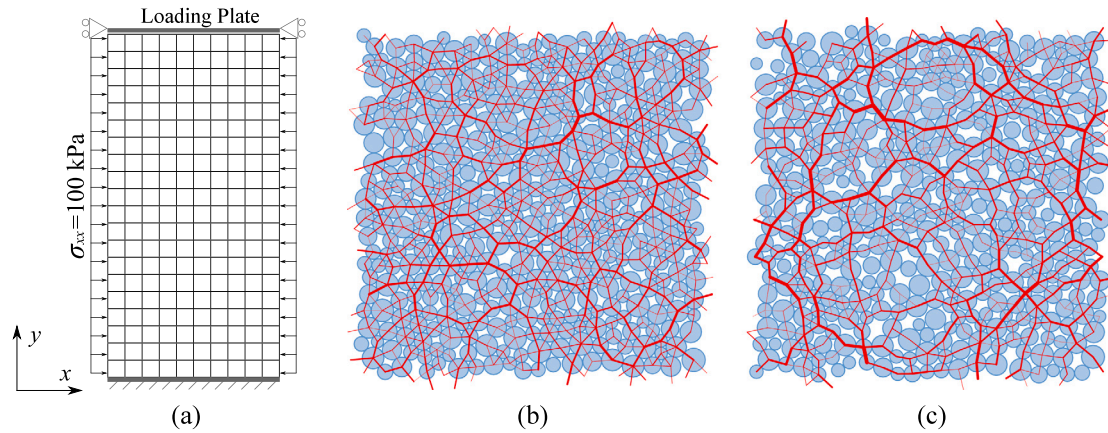
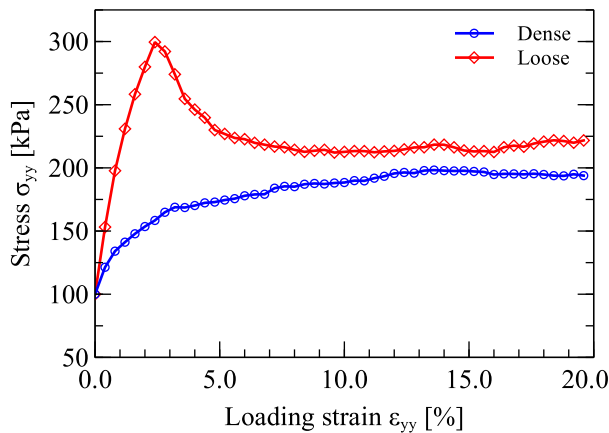**Fig. 12.** (a) Mesh, (b) Dense RVE packing, and (c) Loose RVE packing.

Fig. 13. Evolution of the vertical stress σ_{yy} on the loading plate with the loading strain ϵ_{yy} for the dense and loose specimens.

(e.g., sands) is simulated to preliminarily showcase the capability of the proposed TM-DEMPM framework. As shown in Fig. 15(a), a 1 m wide silo with an opening of 0.2 m is placed 1 m above the ground. A granular sample discretized by 1088 material points with four material points for each cell (0.05 m × 0.05 m) is filled into the silo, and is then discharged freely through the hopper under gravity ($g = 9.8$ m/s^2) (denoted as free discharge). In addition to free discharge under gravity, a comparison case denoted by forced discharge, as shown in Fig. 15(b), is presented to simulate forced granular flow by a loading plate pushing down with a constant downward velocity $v = 0.2$ m/s. Note that the gravity is also applied in the forced discharge case. Both silo walls and ground are assumed to be rigid with a constant frictional coefficient of 0.5.

For simplicity without losing generality, the same material properties as for the biaxial compression tests in Section 5.3.1 are selected, and the RVE packing with a void ratio of 0.243 (see Fig. 15(b)) is prepared after consolidation with a confining stress of 10 kPa. It is worth noting that the confining stress is selected with a similar average stress level within the granular material under gravity. The damping α_p, α_g and the PIC fraction α_{PIC} are all set to 0.1. The simulations run for 12 s and 2 s with a fixed timestep of 1×10^{-4} s for the free and forced discharges, respectively.

Fig. 16 shows the sequential snapshots of discharging processes for the free and forced cases. It is evident that the forced case discharges much faster than the free one, accompanied by a larger increase in temperature. Specifically, the most heated part is found near the hopper outlet for the free discharge, while the silo core is heated more

significantly for the forced discharge due to the compression exerted by the loading plate. Moreover, it appears that the declined walls at the hopper outlet is heated severely. These observations are qualitatively consistent with the simulations by thermally-coupled pure DEM in the literature (Nguyen et al., 2009). Furthermore, the RVE deformation at the two points of interest (A and B in Fig. 15) is tracked and shown in Fig. 17 for the final states. Notably, RVEs A and B suffer from considerably different deformations for both discharge cases, where RVE A remains in the silo while RVE B stays on the ground at different stress levels. RVE A is sheared more severely in the forced discharge due to an external compression, compared with that in the free discharge. As for RVE B which is situated near the base center (symmetric axis) of the granular heap on the ground, the domain is extremely slender with a slight skew.

5.3.3. Melting induced column collapse

In addition to heat generation due to friction dissipation, heat can in turn influence the granular structure through thermal induced expansion/contraction of grains as demonstrated in our benchmark tests in Section 5.1 and melting/weakening of inter-particle cementation in 'icy' granular media. For simplicity, a thermally induced melting model of 'icy' contacts is introduced and applied to column collapse tests in this section. The inter-particle cementation is modeled by a bond contact model with strength sensitive to temperature as given in Section 3.2.3.

To offer a preliminary understanding on how the strength parameter β_b affects the macroscopic strength of a specimen, three groups of biaxial compression tests are conducted with a confining stress of 10, 25 and 50 kPa, respectively, where the selected confining stresses are consistent with the stress level within the granular column in the following column collapse tests. The corresponding RVE packings to these three confining stresses are prepared with the same protocol and material parameters in Section 5.3.1, with a consolidated void ratio of 0.251, 0.240 and 0.232, respectively, which can be regarded as medium-dense specimens. Note that the bond contact model is not activated until the consolidation procedure ends in the specimen preparation, and the bonds are installed only at contacts with non-zero contact forces. However, a complete sensitivity analysis for the bond contact model is beyond the scope of this study. We simply set the bond strength parameter β_b to be [0, 0.01, 0.02] for the three tests in each group ($\beta_b = 0$ for no bonds), whereas μ_b is fixed to 0.5 throughout the rest of this section.

Fig. 18 shows the evolution of the vertical stress σ_{yy} on the loading plate with different bond strength parameter β_b for the three confining stress cases. It is evident that both the peak and residual stresses increase with the bond strength parameter β_b for a given confining stress. The specimen initially with no bonds ($\beta_b = 0$) experiences
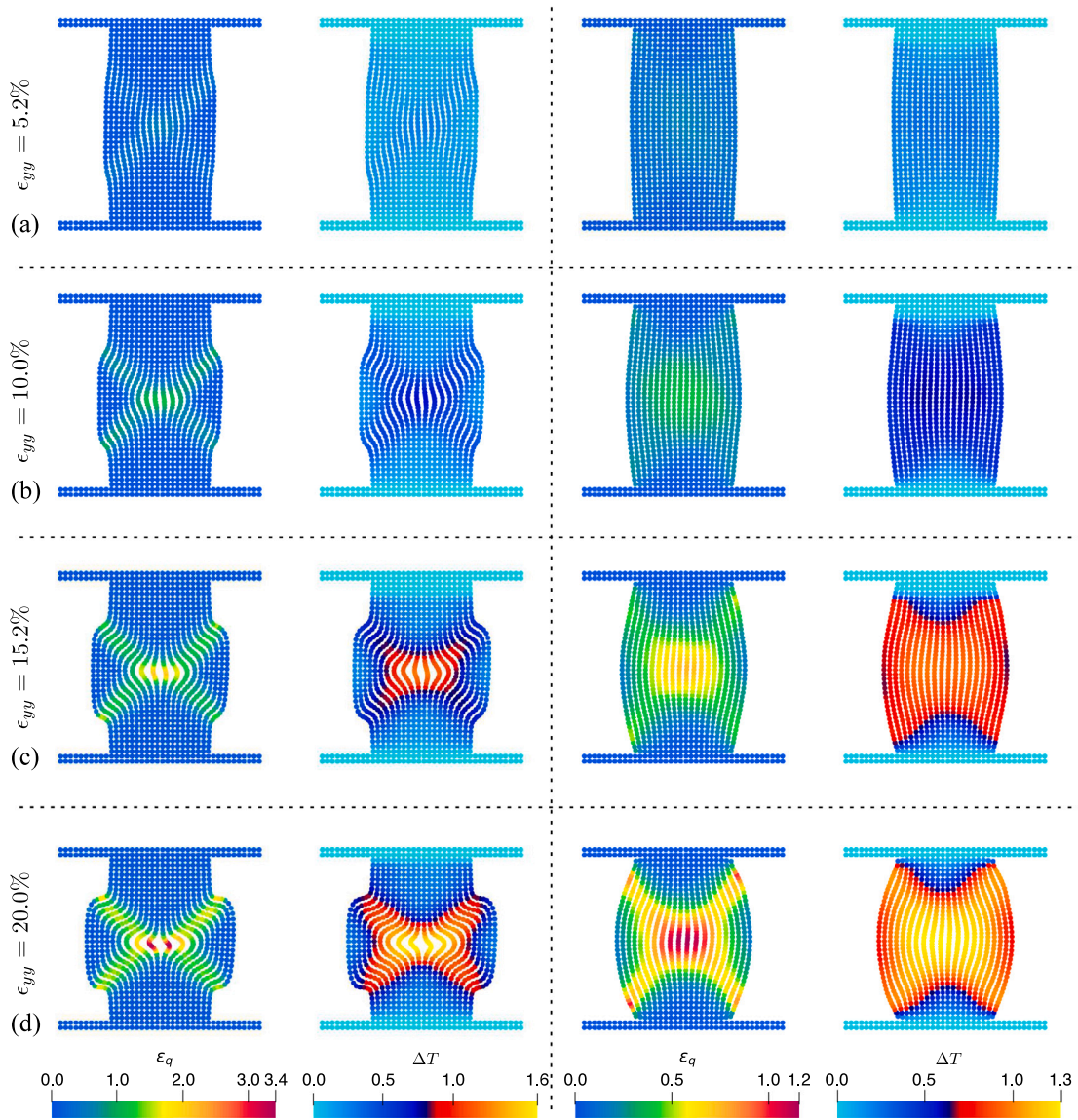
Fig. 14. Evolution of shear bands with deviatoric strain ϵ_q and temperature ΔT (°C) for the dense (left) and loose (right) specimens during shearing.
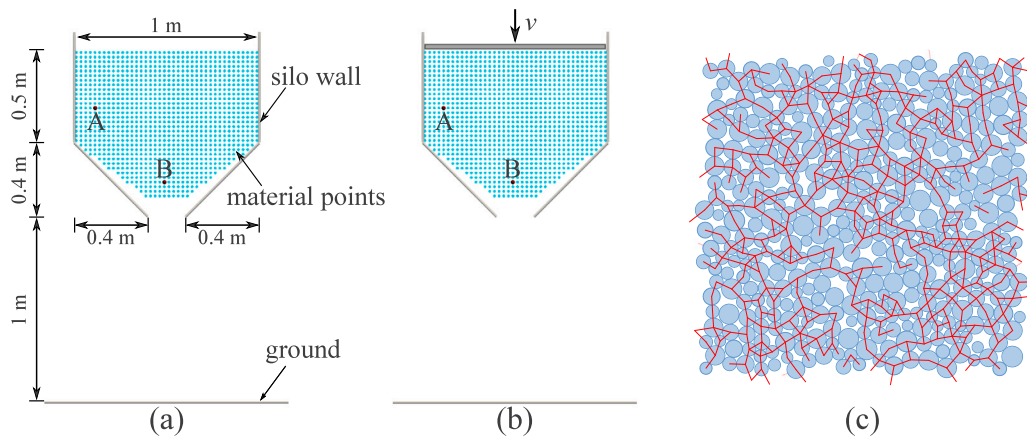

Fig. 15. Illustration of simulation setup of granular silo discharging: (a) free discharge, (b) forced discharge and (c) the initial RVE packing. A and B are two points of interest for tracking. Note: the background grid is not shown in (a) and (b).

a mild stress softening before approaching a critical state, while the strength-enhanced specimens initially with bonds have a marked stress softening. In addition to the enhanced peak stress, one more feature of the initially bonded specimens is exhibited by their residual stress or
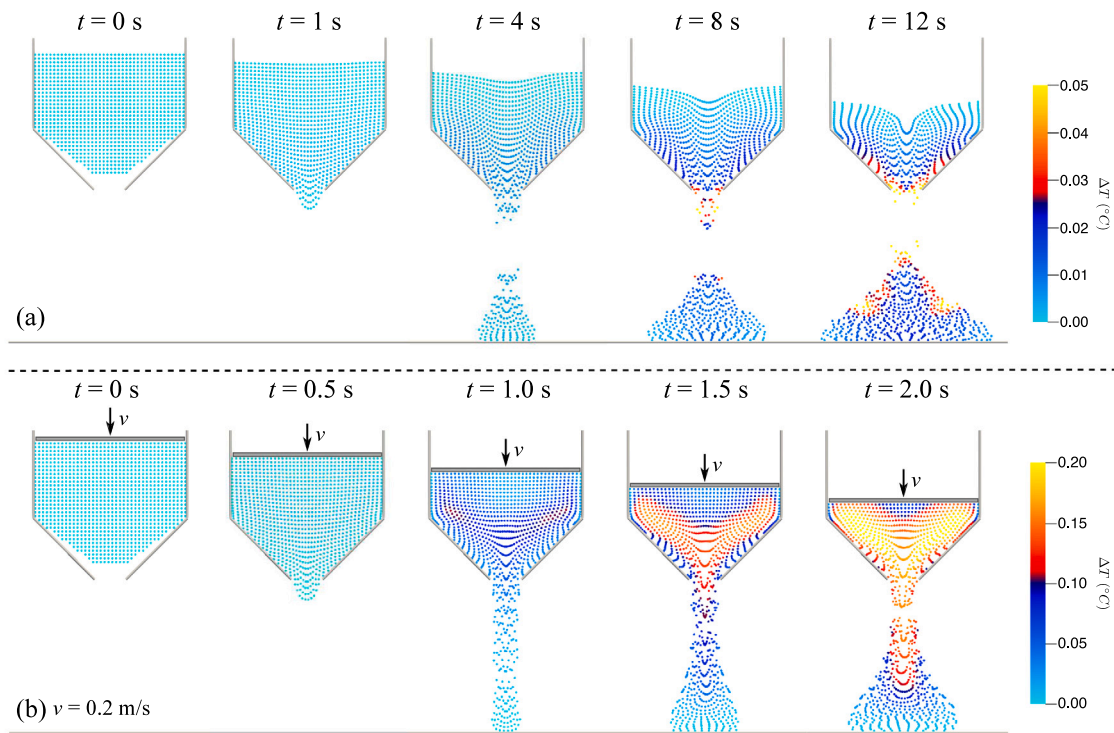
Fig. 16. Temperature increase ΔT in a granular silo during discharging: (a) free discharge and (b) forced discharge.
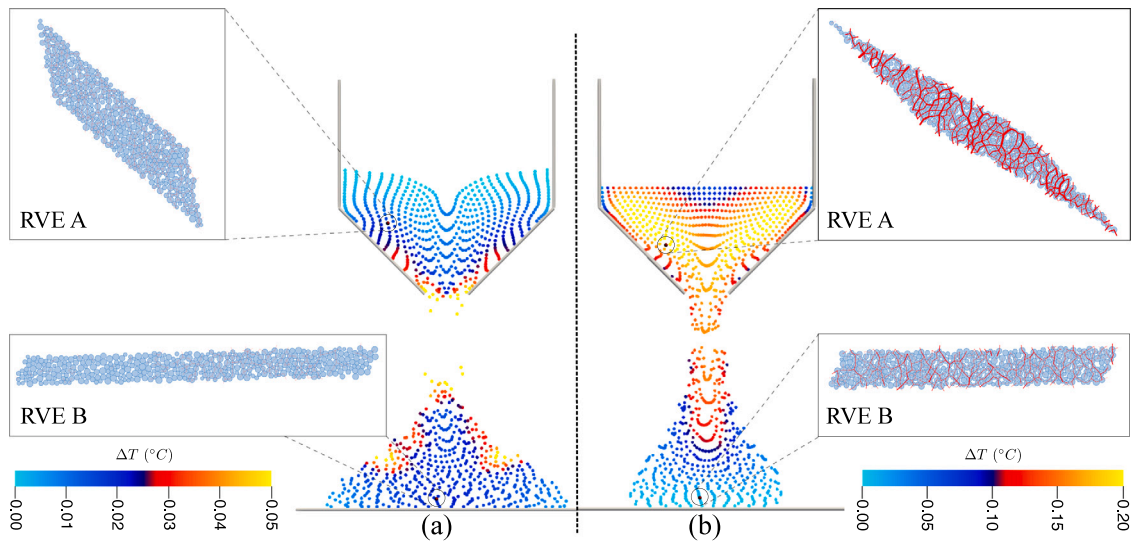
Fig. 17. Configuration of deformed RVEs with contact force networks at points A and B for (a) free discharge and (b) forced discharge.

critical stress. With a larger confining stress, the bonds are more prone to breakage, thereby the residual stress is likely approaching to that of the specimen without bonds, e.g., by comparing the specimens ($\beta_b = 0$ and 0.01) in Fig. 18(c).

To simulate the column collapse test, the simulation setup is illustrated in Fig. 19 with the following protocol. A granular column with a dimension of 2 m × 2 m is set to stand on a frictional ground (friction coefficient of 0.5) confined by two lateral plates: one heating plate on the left that will maintain a constant temperature, and one removable plate on the right that will be removed to trigger the collapse of a column. The entire domain of the granular column is discretized into 20-by-20 cells with four material points in each. Identical RVE packings with a confining stress of 10 kPa are attached to these material

points. In the presence of gravity ($g = 9.8$ m/s^2), the granular column experiences a small settlement to reach a state of static equilibrium with a lateral confinement. It is worth noting that the contact bonds are inactivated during the course of self-weight equilibrium. After that, collapse is triggered by removing the plate on the right side while the heating temperature and the bond strength are activated.

For simplicity, the heating temperature is set to 50 °C, and the threshold temperature T_s is set to 10 °C, see Eq. (40), that is associated to the bond strength parameter β_b. The heat capacity and initial heat conductivity are set to 1 J/(kg K) and 100 W/(m K), respectively. The other material properties adopt the same values as in Section 5.3.1. Five column collapse tests are conducted with different bond strength parameters $\beta_b = 0$, 0.02, and 0.1. Depending on whether the bonds
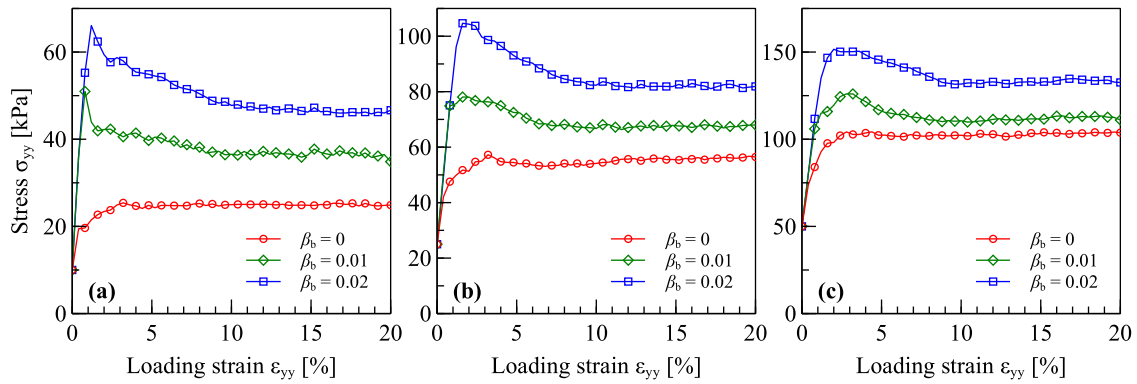
Fig. 18. Evolution of the vertical stress σ_{yy} on the loading plate with the loading strain ϵ_{yy} with different bond strength parameter β_b at a confining stress of (a) 10 kPa, (b) 25 kPa and (c) 50 kPa.
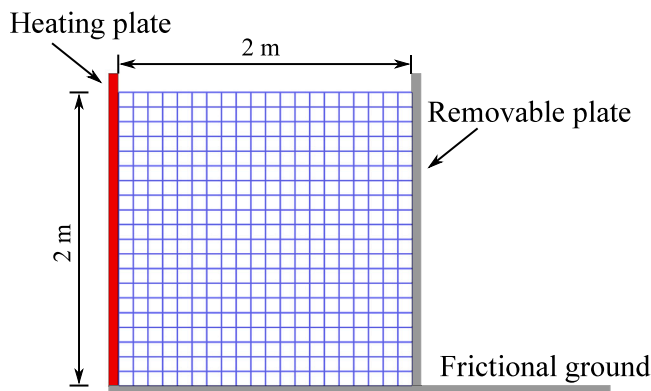

Fig. 19. Simulation setup for column collapse tests.

are meltable or not, cases are denoted as 'melting' or 'no melting', respectively ('melting' means that β_b varies with temperature). For the case without bonds ($\beta_b = 0$), neither 'melting' nor 'no melting' is applicable. The PIC fraction α_{PIC} is set to 0.01. A fixed timestep of 1×10^{-4} s is employed, and simulations run 3 s and 20 s for cases with $\beta_b = 0$ and $\beta_b \neq 0$, respectively.

The evolution of normalized mechanical energy and the snapshots of the columns during collapse are shown in Figs. 20 and 21, respectively. The potential energy $E_p = \sum_{i=1}^{N} m_i g h_i$ and the kinetic energy $E_k = \sum_{i=1}^{N} 0.5 m_i v_i^2$ are normalized by the initial potential energy, where m_i, v_i and h_i are the mass, velocity and position (with the ground as the datum) of the ith material point, and N is the total number of material points. Compared with the cases of 'no melting' in Fig. 20, in the presence of inter-particle bonds, a granular column can have sufficient tensile strength to maintain its stability after the right plate is removed. Specifically, for $\beta_b = 0$, slumping mass experiences a significant increase in kinetic energy immediately after the right plate is removed, before the material reaches a perfectly straight slope as shown in Fig. 21(a). By contrast, a sudden failure occurs when the plastic deformation develops to some degree in the 'no melting' case of $\beta_b = 0.02$ as an example. A column can be stable when the bond-enhanced tensile strength is sufficiently large, see the 'no melting' case of $\beta_b = 0.1$.

As for the melting cases, the inter-particle bonds can 'melt' as a function of temperature in the thermal field, where the behavior of a granular column may be significantly different from the 'no melting' cases. Taking the case $\beta = 0.02$ in Fig. 20 as an example, both 'melting' and 'no melting' columns undergo collapse once the right plate is

removed, both experiencing almost identical energy evolution during the beginning 3 s. After that, the behaviors become divergent with the contribution of thermal field, where the 'melting' case exhibits a lower potential energy. In other words, the 'melting' has a minor effect on the collapse process during the beginning 3 s due to the less-enhanced column, e.g., the case $\beta_b = 0.02$, see Fig. 21(b). However, for highly-enhanced columns, e.g., $\beta_b = 0.1$, a sudden failure occurs when the bonds 'melt' completely near the heat source side at around 15 s, see Figs. 20 and 21(c).

6. Summary

We proposed a novel hierarchical multiscale computational framework, TM-DEMPM, for effective simulation of complex thermo-mechanical (TM) coupling responses of granular media undergoing large deformation or flow. As a significant extension of our previous work based on coupled FEM with DEM for small strain problems, this new framework leverages the strength of both continuum-based MPM and micromechanics-based DEM. It is demonstrated that the new TM-DEMPM can effectively capture a variety of fundamental TM behaviors of granular media, such as thermally induced stress, mechanically induced heat and thermally induced melting, from a physics-informed scale-crossing perspective as outlined below:

- The thermally induced stress can be physically modeled by the expansion or contraction of individual particles.
- The mechanically induced heat is associated to the inter-particle friction dissipation at the microscopic scale.
- The thermally induced melting is captured by a temperature-sensitive bond contact model at the microscopic scale, which conveniently serves as a bridge for the macroscopic deformation and thermal conduction.

The proposed framework has been rigorously benchmarked before being successfully applied to simulating three selected problems, including heat generation in biaxial compression tests, free and forced discharge of granular silos, and column collapse of 'icy' granular media, as representative examples of the three features mentioned above, respectively.

The proposed framework has a broad range of potential fields of application, such as energy pile design, slope stability analysis in permafrost areas, grain storage in agricultural industry, and powder tabletting in pharmaceutical industry. In practice, nevertheless, it is common to encounter the involvement fluid within granular media. It would be interesting to further extend the proposed framework to consider the thermo-hydro-mechanical (THM) coupling as an all-in-one toolkit. Moreover, although the formulation has been presented in 2D,
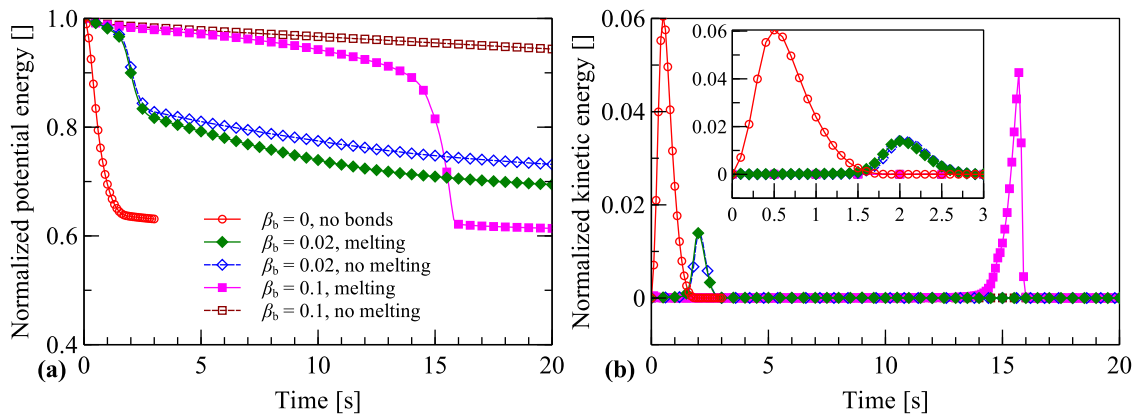
Fig. 20. Evolution of mechanical (potential and kinetic) energy normalized by the initial potential energy during collapse.

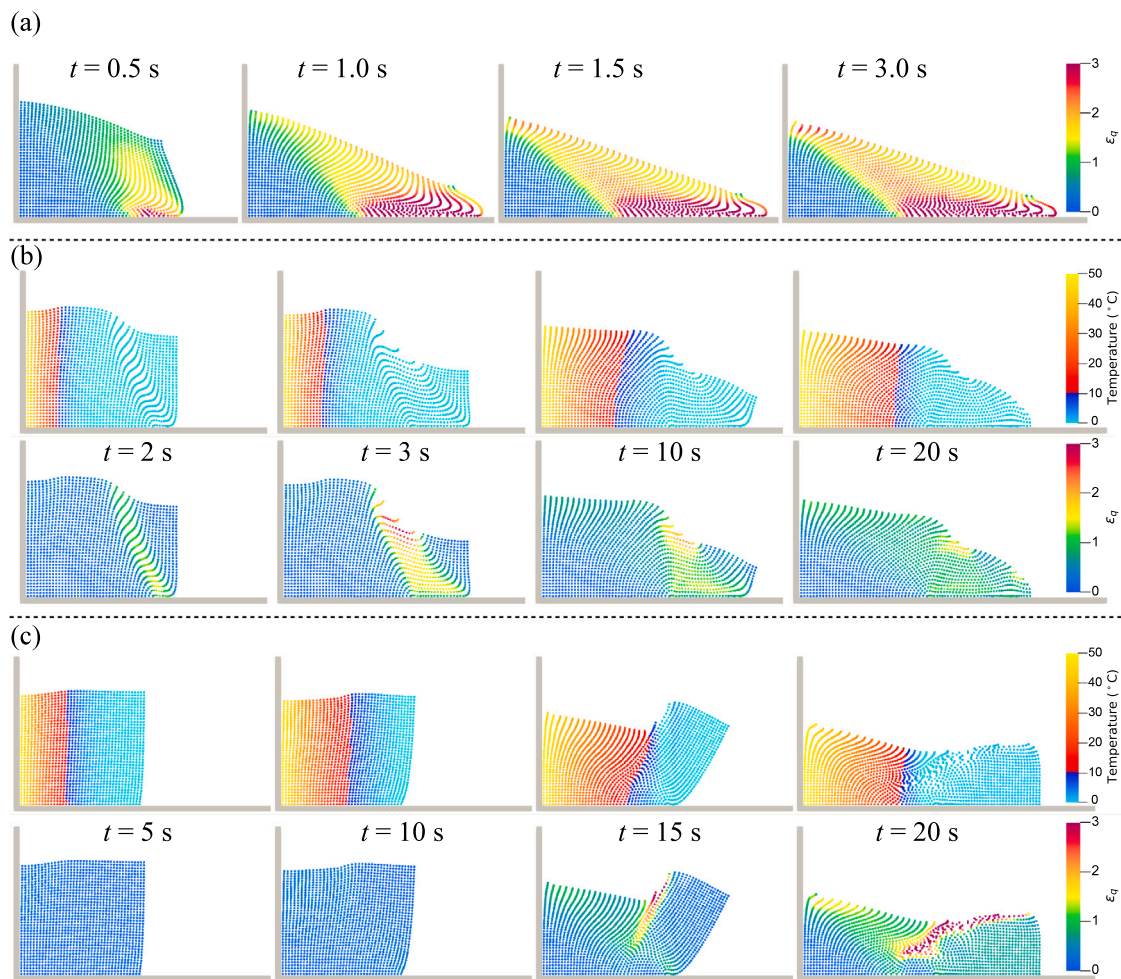**Fig. 21.** Snapshots of column collapse tests for (a) $\beta_b = 0$, no bonds, (b) $\beta_b = 0.02$, melting, and $\beta_b = 0.1$, melting.

the proposed framework can be readily extended for 3D simulations. It is also noteworthy that though the proposed staggered algorithm for thermo-mechanical coupling adopts the same timestep for both the thermal and mechanical solvers in the present study, it is indeed flexible to choose different timesteps, which can be effective and useful in simulating practical problems that involve significant differences in time scale between thermal conduction and mechanical deformation.

CRediT authorship contribution statement

Shiwei Zhao: Conceptualization, Methodology, Software, Writing – original draft. **Jidong Zhao:** Supervision, Methodology, Writing – review & editing, Resources. **Weijian Liang:** Writing – review & editing. **Fujun Niu:** Supervision, Resources.

Declaration of competing interest

The authors declare that they have no known competing financial interests or personal relationships that could have appeared to influence the work reported in this paper.

Acknowledgments

References

Andrade, J.E., Avila, C., Hall, S.A., Lenoir, N., Viggiani, G., 2011. Multiscale modeling and characterization of granular matter: from grain kinematics to continuum mechanics. J. Mech. Phys. Solids 59, 237–250.

Balla, M., 1991. Analytical study of the thermal shock problem of a half-space with various thermoelastic models. Acta Mech. 89, 73–92.

Bardenhagen, S.G., Kober, E.M., 2004. The generalized interpolation material point method. Comput. Model. Eng. Sci. 5, 477–496.

Becattini, V., Motmans, T., Zappone, A., Madonna, C., Haselbacher, A., Steinfeld, A., 2017. Experimental investigation of the thermal and mechanical stability of rocks for high-temperature thermal-energy storage. Appl. Energy 203, 373–389.

Brackbill, J.U., Ruppel, H.M., 1986. Flip: A method for adaptively zoned. particle-in-cell calculations of fluid flows in two dimensions. J. Comput. Phys. 65, 314–343.

Brown, N.J., Chen, J.-F., Ooi, J.Y., 2014. A bond model for DEM simulation of cementitious materials and deformable structures. Granul. Matter 16, 299–311.

Bui, H.H., Fukagawa, R., Sako, K., Ohno, S., 2008. Lagrangian meshfree particles method (sph) for large deformation and failure flows of geomaterial using elastic–plastic soil constitutive model. Int. J. Numer. Anal. Methods Geomech. 32, 1537–1570.

Caulk, R., Sholtès, L., Krzaczek, M., Chareyre, B., 2020. A pore-scale thermo–hydro–mechanical model for particulate systems. Comput. Methods Appl. Mech. Engrg. 372, 113292.

Chen, Q., Andrade, J.E., Samaniego, E., 2011. AES for multiscale localization modeling in granular media. Comput. Methods Appl. Mech. Engrg. 200, 2473–2482.

Choo, J., Kim, Y.J., Lee, T.S., Lee, J., Kim, Y.S., 2013. Stress-induced evolution of anisotropic thermal conductivity of dry granular materials. Acta Geotech. 8, 91–106.

Christoffersen, J., Mehrabadi, M.M., Nemat-Nasser, S., 1981. A micromechanical description of granular material behavior. J. Appl. Mech. 48, 339–344.

Cundall, P.A., Strack, O.D., 1979. A discrete numerical model for granular assemblies. Géotechnique 29, 47–65.

Danilouskaya, V., 1950. Thermal stresses in elastic half space due to sudden heating of its boundary, 14, 316–318.

de Vaucorbeil, A., Nguyen, V.P., Sinaie, S., Wu, J.Y., 2020. Chapter Two - Material Point Method After 25 Years: Theory, Implementation, and Applications. In: Advances in Applied Mechanics, vol. 53, Elsevier, pp. 185–398.

Desrues, J., Argilaga, A., Caillerie, D., Combe, G., Nguyen, T.K., Richefeu, V., Pont, S.D., 2019. From discrete to continuum modelling of boundary value problems in geomechanics: an integrated FEM-DEM approach. Int. J. Numer. Anal. Methods Geomech. 43, 919–955.

Dong, Y., Wang, D., Randolph, M.F., 2015. A GPU parallel computing strategy for the material point method. Comput. Geotech. 66, 31–38.

Evans, T.M., Frost, J.D., 2010. Multiscale investigation of shear bands in sand: physical and numerical experiments. Int. J. Numer. Anal. Methods Geomech. 34, 1634–1650.

Froitzheim, N., Majka, J., Zastrozhnov, D., 2021. Methane release from carbonate rock formations in the siberian permafrost area during and after the 2020 heat wave. Proc. Natl. Acad. Sci. 118.

Gan, Y., Rognon, P., Einav, I., 2012. Phase transitions and cyclic pseudotachylyte formation in simulated faults. Phil. Mag. 92, 3405–3417.

Gingold, R.A., Monaghan, J.J., 1977. Smoothed particle hydrodynamics: theory and application to non-spherical stars. Mon. Not. R. Astron. Soc. 181, 375–389.

Guo, N., Yang, Z., Yuan, W., Zhao, J., 2021. A coupled SPFEM/DEM approach for multiscale modeling of large-deformation geomechanical problems. Int. J. Numer. Anal. Methods Geomech. 45, 648–667.

Guo, N., Zhao, J., 2013. The signature of shear-induced anisotropy in granular media. Comput. Geotech. 47, 1–15.

Guo, N., Zhao, J., 2014. A coupled FEM/DEM approach for hierarchical multiscale modelling of granular media. Internat. J. Numer. Methods Engrg. 99, 789–818.

Hammerquist, C.C., Nairn, J.A., 2017. A new method for material point method particle updates that reduces noise and enhances stability. Comput. Methods Appl. Mech. Engrg. 318, 724–738.

Harlow, F.H., 1964. The particle-in-cell computing method for fluid dynamics. Methods Comput. Phys. 3, 319–343.

Herrmann, H.J., Hovi, J.-P., Luding, S., 2013. Physics of Dry Granular Media, vol. 350, Springer Science & Business Media.

Hyodo, M., Li, Y., Yoneda, Y., Yoshimoto, N., Nishimura, A., 2014. Effects of dissociation on the shear strength and deformation behavior of methane hydrate-bearing sediments. Mar. Pet. Geol. 51, 52–62.

Krok, A., Garcia-Trinanes, P., Peciar, M., Wu, C.-Y., 2016. Finite element analysis of thermomechanical behaviour of powders during tabletting. Chem. Eng. Res. Des. 110, 141–151.

Lei, X., He, S., Abed, A., Chen, X., Yang, Z., Wu, Y., 2021. A generalized interpolation material point method for modelling coupled thermo-hydro-mechanical problems. Comput. Methods Appl. Mech. Engrg. 386, 114080.

Li, X., Yu, H.-S., 2015. Particle-scale insight into deformation noncoaxiality of granular materials. Int. J. Geomech. 15, 04014061.

Liang, W., Zhao, J., 2019. Multiscale modeling of large deformation in geomechanics. Int. J. Numer. Anal. Methods Geomech. 43, 1080–1114.

Liu, E., Lai, Y., Wong, H., Feng, J., 2018. An elastoplastic model for saturated freezing soils based on thermo-poromechanics. Int. J. Plast. 107, 246–285.

Liu, C., Sun, Q., Yang, Y., 2017. Multi-scale modelling of granular pile collapse by using material point method and discrete element method. Procedia Eng. 175, 29–35.

Liu, Y., Sun, W., Yuan, Z., Fish, J., 2016. A nonlocal multiscale discrete-continuum model for predicting mechanical behavior of granular materials. Internat. J. Numer. Methods Engrg. 106, 129–160.

Luding, S., 2004. Micro–macro transition for anisotropic, frictional granular packings. Int. J. Solids Struct. 41, 5821–5836.

Luong, M.-P., 2007. Introducing infrared thermography in soil dynamics. Infrared Phys. Technol. 49, 306–311.

Maslin, M., Owen, M., Betts, R., Day, S., Dunkley Jones, T., Ridgwell, A., 2010. Gas hydrates: past and future geohazard? Philos. Trans. R. Soc. Lond. Ser. A Math. Phys. Eng. Sci. 368, 2369–2393.

Meille, S., Garboczi, E.J., 2001. Linear elastic properties of 2D and 3D models of porous materials made from elongated objects. Modelling Simulation Mater. Sci. Eng. 9, 371.

Michalowski, R.L., Zhu, M., 2006. Frost heave modelling using porosity rate function. Int. J. Numer. Anal. Methods Geomech. 30, 703–722.

Moscardini, M., Gan, Y., Pupeschi, S., Kamlah, M., 2018. Discrete element method for effective thermal conductivity of packed pebbles accounting for the smoluchowski effect. Fusion Eng. Des. 127, 192–201.

Na, S., Sun, W., 2017. Computational thermo-hydro-mechanics for multiphase freezing and thawing porous media in the finite deformation range. Comput. Methods Appl. Mech. Engrg. 318, 667–700.

Nairn, J.A., 2015. Numerical simulation of orthogonal cutting using the material point method. Eng. Fract. Mech. 149, 262–275.

Nguyen, V., Cogné, C., Guessasma, M., Bellenger, E., Fortin, J., 2009. Discrete modeling of granular flow with thermal transfer: application to the discharge of silos. Appl. Therm. Eng. 29, 1846–1853.

Onsager, L., 1931. Reciprocal relations in irreversible processes. I. Phys. Rev. 37, 405.

Pintaldi, S., Perfumo, C., Sethuvenkatraman, S., White, S., Rosengarten, G., 2015. A review of thermal energy storage technologies and control approaches for solar cooling. Renew. Sustain. Energy Rev. 41, 975–995.

Radjai, F., 2018. Multi-periodic boundary conditions and the contact dynamics method. C. R. Méc. 346, 263–277.

Russo, P., De Rosa, A., Mazzaro, M., 2017. Silo explosion from smoldering combustion: a case study. Can. J. Chem. Eng. 95, 1721–1729.

Sadeghirad, A., Brannon, R.M., Burghardt, J., 2011. A convected particle domain interpolation technique to extend applicability of the material point method for problems involving massive deformations. Internat. J. Numer. Methods Engrg. 86, 1435–1456.

Sadeghirad, A., Brannon, R.M., Guilkey, J., 2013. Second-order convected particle domain interpolation (cpdi2) with enrichment for weak discontinuities at material interfaces. Internat. J. Numer. Methods Engrg. 95, 928–952.

Sani, A.K., Singh, R.M., Amis, T., Cavarretta, I., 2019. A review on the performance of geothermal energy pile foundation, its design process and applications. Renew. Sustain. Energy Rev. 106, 54–78.

Saruwatari, M., Nakamura, H., 2022. Coarse-grained discrete element method of particle behavior and heat transfer in a rotary kiln. Chem. Eng. J. 428, 130969.

Shen, Z., Jiang, M., Thornton, C., 2016. DEM simulation of bonded granular material. Part I: Contact model and application to cemented sand. Comput. Geotech. 75, 192–209.

Stomakhin, A., Schroeder, C., Chai, L., Teran, J., Selle, A., 2013. A material point method for snow simulation. ACM Trans. Graph. 32, 1–10.

Sulsky, D., Zhou, S.-J., Schreyer, H.L., 1995. Application of a particle-in-cell method to solid mechanics. Comput. Phys. Comm. 87, 236–252.

Tao, J., Zheng, Y., Chen, Z., Zhang, H., 2016. Generalized interpolation material point method for coupled thermo-mechanical processes. Int. J. Mech. Mater. Des. 12, 577–595.

Thornton, C., 2000. Numerical simulations of deviatoric shear deformation of granular media. Géotechnique 50, 43–53.

Vargas, W.L., McCarthy, J.J., 2007. Thermal expansion effects and heat conduction in granular materials. Phys. Rev. E 76, 041301.

Wren, J.R., Borja, R.I., 1997. Micromechanics of granular media part II: Overall tangential moduli and localization model for periodic assemblies of circular disks. Comput. Methods Appl. Mech. Engrg. 141, 221–246.

Yang, W., Zhou, Z., Pinson, D., Yu, A., 2014. Periodic boundary conditions for discrete element method simulation of particle flow in cylindrical vessels. Ind. Eng. Chem. Res. 53, 8245–8256.

Zhai, C., Herbold, E., Hall, S., Hurley, R., 2019. Particle rotations and energy dissipation during mechanical compression of granular materials. J. Mech. Phys. Solids 129, 19–38.

Zhang, D.Z., Ma, X., Giguere, P.T., 2011. Material point method enhanced by modified gradient of shape function. J. Comput. Phys. 230, 6379–6398.

Zhang, N., Wang, Z., 2017. Review of soil thermal conductivity and predictive models. Int. J. Therm. Sci. 117, 172–183.

Zhang, H., Yuan, H., Trias, F.X., Yu, A., Tan, Y., Oliva, A., 2016. Particulate immersed boundary method for complex fluid–particle interaction problems with heat transfer. Comput. Math. Appl. 71, 391–407.

Zhao, S., Evans, T.M., Zhou, X., 2018. Effects of curvature-related DEM contact model on the macro-and micro-mechanical behaviours of granular soils. Géotechnique 68, 1085–1098.

Zhao, S., Evans, T.M., Zhou, X., Zhou, S., 2017. Discrete element method investigation on thermally-induced shakedown of granular materials. Granul. Matter 19 (11).

Zhao, T., Feng, Y.T., 2019. An enthalpy based discrete thermal modelling framework for particulate systems with phase change materials. Powder Technol. 354, 505–516.

Zhao, S., Zhao, J., Lai, Y., 2020. Multiscale modeling of thermo-mechanical responses of granular materials: A hierarchical continuum–discrete coupling approach. Comput. Methods Appl. Mech. Engrg. 367, 113100.

Zhao, S., Zhao, J., Liang, W., 2021. A thread-block-wise computational framework for large-scale hierarchical continuum-discrete modeling of granular media. Internat. J. Numer. Methods Engrg. 122, 579–608.